Nanostructures in metal films for enhanced transmission and polarization controlled diffraction

by

Pramodha Marthandam
B.E., Anna University, 2005

A Thesis Submitted in Partial Fulfillment
of the Requirements for the Degree of

MASTER OF APPLIED SCIENCE

in the Department of Electrical and Computer Engineering

Supervisory Committee

Nanostructures in metal films for enhanced transmission and polarization controlled diffraction

By
Pramodha Marthandam
B.E., Anna University, 2005.

Dr. Reuven Gordon, Supervisor
Department of Electrical and Comupter Engineering

Dr. Harry Kwok, Departmental Member
Department of Electrical and Comupter Engineering

Dr. Alexandre Brolo, Outside Member
Department of Chemistry

Abstract

Supervisory Committee
Dr. Reuven Gordon, Supervisor
Department of Electrical and Comupter Engineering

Dr. Harry Kwok, Departmental Member
Department of Electrical and Comupter Engineering

Dr. Alexandre Brolo, Outside Member
Department of Chemistry

A novel nano-structure is proposed to enhance extraordinary optical transmission from a periodic array of nano-holes. The Plasmonic Bragg reflector works by recapturing surface plasmons that are scattered off the edge of the array during the extraordinary optical transmission process, and reflecting them back towards the array where they can interfere with the light and enhance transmission. This reduces losses from a sub-wavelength aperture array. The reflectors are positioned to reflect in-phase with the light transmission. Polarization sensitivity of the plasmonic Bragg reflector is demonstrated. Modulation of the transmission is achieved by varying the separation between the array and reflectors. Isolation of adjacent structures on a plasmonic device by the use of the Bragg reflectors is attempted.

Transmission and diffraction properties of quasiperiodic nano-hole arrays in a gold film are studied. Resonant transmission is observed, whose values do not simply match surface plasmon wave-vector values. Rotationally symmetric diffraction from the quasicrystal nano-hole array. This diffraction is seen to be controllable by the polarization of the excitation laser. Finite difference time domain calculations of the quasiperiodic array are performed to better understand the origin of the observed transmission resonances. Good agreement between theory and experiment is observed. Calculations show the formation of near-field hot-spots over the structure.

Table of Contents

List of Figures

Acknowledgments

I thank my supervisor Dr. Reuven Gordon for his support and encouragement throughout the duration of this project, and for permitting me to carry out extensive experiments.

I thank Dr. Alexandre Brolo, Department of Chemistry and Dr. David Sinton, Department of Mechanical Engineering for valuable discussions.

I thank all my colleagues in the optics lab for their encouragement and valuable inputs.

I thank Vikram and Suji for helping me come this far, and my parents for their love and prayers.

This thesis is dedicated to my brother Vikram and my parents, for it is their love that made this possible.

Chapter 1

Introduction

1.1 Sub-wavelength optics and plasmonics

Sub-wavelength optics and nano-optics refer to the branch of optics that deals with the interaction of light and matter at dimensions smaller than the wavelength of light. Miniaturization of photonic devices to sub-wavelength scales limited by the diffraction limit [1]. Plasmonic devices have the potential to overcome this diffraction limit. Plasmons are the oscillations of free electron gas at optical frequencies. Surface plasmons (SPs) are the oscillation of free electrons at the interface of a metal and a dielectric. By employing geometries of conductors and dielectrics, modes can be created at optical frequencies with effective indices of refraction that are much larger than those of the constituent materials themselves. Due to the high effective index and because these waves are mediated by electrons rather than optical fields, confinement of light to dimensions in the deep sub-wavelength regime can be achieved by plasmonics. Therefore, plasmonics offers the ability to merge the progressively diminishing device sizes, better than that of electronics, and the high speeds offered by photonics [2]. Plasmonics also offers the ability to densely integrate components.

SPs have been known to aid the transmission of light through sub-wavelength apertures leading to extra-ordinary optical transmission (EOT). Due to the possibility of focusing fields to very tight spots, localization of fields is possible. Due to the surface nature of SPs, they can be harnessed in applications like surface enhanced Raman spectroscopy (SERS) and surface enhanced fluorescence spectroscopy (SEFS). Due to their ability to enhance local fields, SPs are very useful in applications that need very high field intensities, such as second harmonic generation (SHG), whose performance varies as the square of the field intensity, and sensing applications, where the sensitivity is affected by the fields. EOT through sub-wavelength apertures and the high field intensities and localized fields due to SPs , can make sub-wavelength hole arrays ideal substrates for all

the above-mentioned applications such as SERS, SHG, and various other spectroscopic and sensing applications.

1.2 Research objectives

While EOT, far higher than predicted is seen from periodic arrays of sub-wavelentgh apertures, SPs that contribute to EOT also scatter away from the array. This scattering constitutes a loss mechanism, and possible corss-talk between adjacent structures on the same metal substrate. A novel structure is proposed to minimize loss due to this scattering of SPs. These structures, named as plasmonic Bragg reflectors (PBRs) eliminate loss by recapturing scattered SPs, and reflecting them back towards the array. Here, the reflected SPs may interfere with the SPs leading to EOT, thus resulting in enhanced EOT. In order to characterize the capability of these structures to confine SPs as proposed, the structure is designed and fabricated, and tested. The possibility of using PBRs to isolate structures on a plasmonic integrated circuit is explored.

In order to study the actual role of periodicity in EOT, quasiperiodic arrays of nano-holes in a gold film are studied. Multiple transmission resonances are seen in the visible spectrum from these structures. Since SPs propagate in the direction of polarization, the polarization dependence of their diffraction is studied. Finite difference time domain (FDTD) calculations of the quasicrystal are carried out to better understand the physics behind the behaviour of the structure.

1.3 Organization of the thesis

Chapter 2 presents a review of the EOT phenomenon, its origin and the effect of shape of nano-holes on the transmission. Important works on applications of nano-hole arrays to spectroscopy and sensing are reviewed. The motivation behind studying the PBR and quasiperiodic nano-hole arrays are presented

In chapter 3, fabrication of the structures presented in this thesis is discussed. Scanning electron microscopy (SEM) and focused ion beam (FIB) milling techniques are outlined. Creation of structures using script files and stream file inputs to the FIB are explained.

Chapter 4 outlines the transmission and diffraction experiments carried out. Experimental setups and methods are outlined.

In chapter 5, results of experiments on the PBR structure are presented. Polarization sensitivity of the PBR structure is explained. Modulation of transmission by varying the separation between the nano-hole array and PBR is shown. The possibility of using the PBR for isolation is explored. Structures used in on-going isolation measurements are presented.

In chapter 6, results of transmission and diffraction measurements on the quasicrystal nano-hole arrays are presented. Transmission resonances are compared with the resonances obtained by wave-vector matching of the Fourier components. Rotational symmetry and polarization control of the diffraction pattern is demonstrated. Results of FDTD calculations on this structure are shown. Formation of near field hot-spots is demonstrated.

In chapter 7, possible avenues for future works are explored.

Appendix A and B contain the script file and input file used to fabricate the PBR structure. Appendix C contains the script used to fabricate the quasicrystal structure. In appendix D, components of the stream file are explained. In appendix E, the results of attempts at polystyrene self assembly to form nano-hole arrays are presented. In appendix F, results of optical trapping experiments attempted with surface plasmon resonance (SPR) from nano-hole arrays is presented.

Chapter 2

Literature review

Introduction

This chapter outlines past works on EOT from nano-hole arrays, and some important contributions from our research group and collaborators. In section 2.1, surface plasmon resonance, and its excitation are explained in terms of material disperion characteristics. In section 2.2, the extraordinary optical transmission phenomenon is discussed. In section 2.3, the effect of hole shape on the transmission properties is discussed. Effects of elliptical and rectangular holes are explained. Polarization mechanisms are discussed. In section 2.4, nano-holes for high local field intensities are touched upon. In section 2.5, applications of nano-hole arrays in spectroscopic methods such as SERS and SEFS are discussed. In section 2.6, the use of nano-hole arrays in SPR sensors is discussed. In section 2.7, the motivation behind the PBR structure is presented. In section 2.8, the reason for studying the quasipeirodic nano-hole array is explained.

2.1 Surface plasmon resonance

The excitation of SPs can occur by irradiation with photons. The excitation occurs when the energy carried by the photons can be transferred to the electrons in the metal. The fields possessed by the SP waves decay exponentially into the metal and the dielectric. Within the metal, the decay length is dictated by the skin-depth, which is the maximum depth of penetration of electromagnetic fields into the metal. Figure 2.1 schematically depicts SPs between a metal and a dielectric.

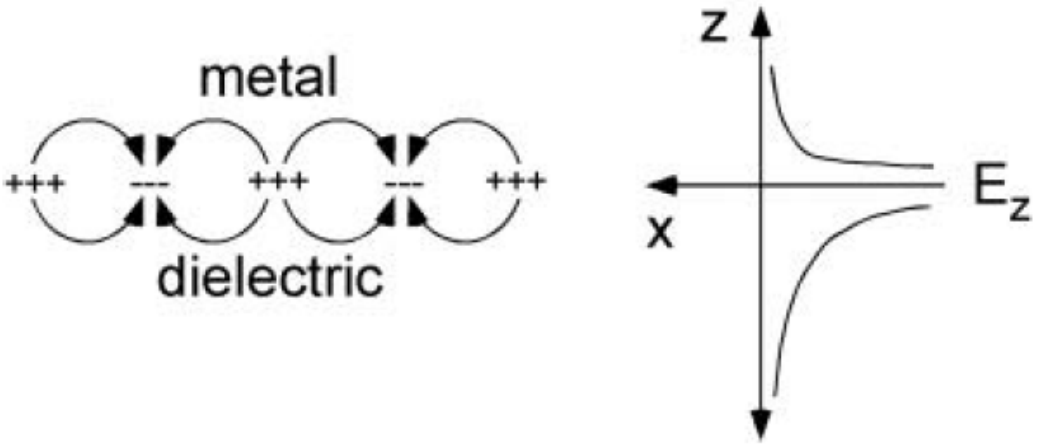

Figure 2.1: Schematic depiction of SPs at the interface of a metal and a dielectric. SP waves propagate in the x direction and decay along the z direction into both materials [3].

Excitation of SPs cannot be achieved simply by irradiating the metal surface with light. This can be understood in terms of the material dispersion characteristics. Figure 2.2 shows the dispersion cirves of SPs at an air-metal interface, and the light line of air. It is clear that the two curves do not have an intersection. For the excitation of SPs. The two curves must intersect. As the SP dispersion always lies to the right of the light line of air, either prism coupling or grating coupling is necessary for photons propagating in air to couple into the SPs. When such coupling is achieved, the two curves will intersect. The wavelength at which this coupling occurs is known the surface plasmon resonance (SPR).

The SP wave vector at resonance is given by [4]:

$$k_{sp} = \frac{\omega}{c}\sqrt{\frac{\varepsilon_m \varepsilon_d}{\varepsilon_m + \varepsilon_d}} \qquad (2.1)$$

Where ω is the frequency at SPR, c is the velocity of light, ε_m is the dielectric constant of the metal and ε_d is the dielectric constant of the surrounding dielectric (in this example, air).

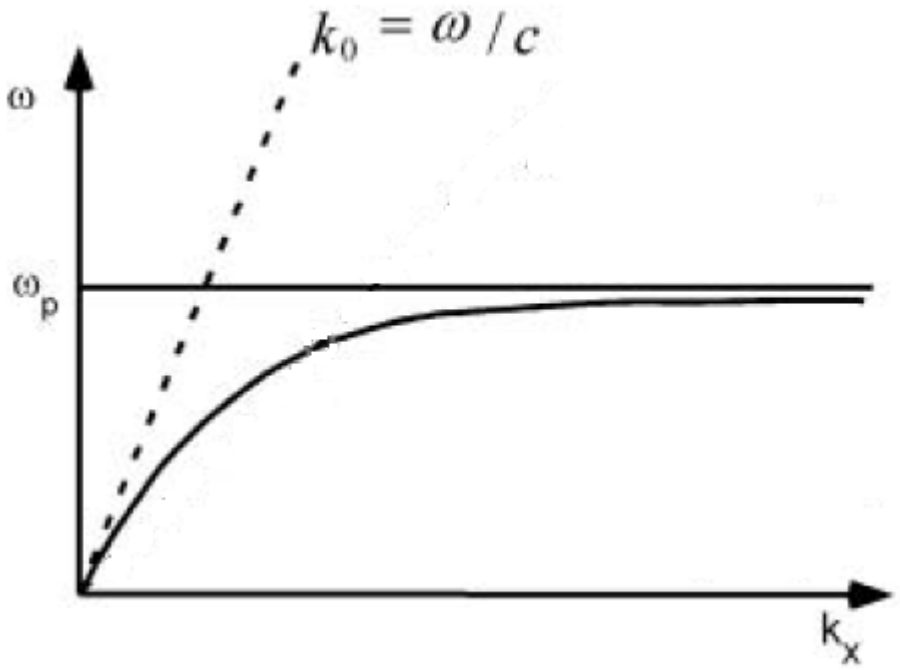

Figure 2.3: SP dispersion curves for the interface of a metal and air. The dashed line is the light line of air. The curve represents the SP dispersion. ω_p is the plasma frequency of the metal [3].

The wave-vector k of an electromagnetic wave propagating in a metal varies with frequency ω [5]:

$$k^2 = \omega^2 \mu\varepsilon\left(1 - \frac{\omega_p^2}{\omega^2}\right) \qquad (2.2)$$

Where ω_p is the plasma frequency of the metal, μ and ε are the permeability and permittivity of the metal at ω.

For frequencies below the plasma frequency, the wave-vector is complex. The complex value of wave-vector, and hence dielectric constant indicates attenuation

2.2 Extraordinary optical transmission

In 1998, Ebbesen et al demonstrated EOT from a periodic lattice of sub-wavelength apertures in an optically thick metal film [6]. This result was contrary to what is known as the Bethe limit, which postulates that transmission through an aperture smaller than the wavelength of light scales as:

$$T \propto \left(\frac{a}{\lambda}\right)^4 \qquad (2.3)$$

where a is the radius of the sub-wavelength aperture and λ is the wavelength of light [7].

Subsequently, EOT was observed in isolated sub-wavelength apertures in metal films as well [8]. Since these discoveries, considerable efforts have been directed towards understanding the mechanisms behind the EOT phenomenon, as it held promise for a myriad of applications including optical filters [9], non-linear optics [10], sub-wavelength lithographic techniques [11] and spectroscopy [12].

Originally, the EOT phenomenon was attributed to the coupling between the incident light and the surface plasmon polaritons (SPPs) or simply SPs. The periodicity of the lattice imposes a Bragg condition for SPR which may be defined mathematically as:

$$\lambda^{SP}(i,j) = p\left(i^2 + j^2\right)^{-1/2} \sqrt{\frac{\varepsilon_m \varepsilon_d}{\varepsilon_m + \varepsilon_d}} \qquad (2.4)$$

where λ^{SP} is the coupling wavelength for SP resonance, p is the periodicity of the array and i, j are integers indicating the scattering order of the grating [6], [13].

The EOT phenomenon was observed in the visible range for metals that supported SPs, and not observed for materials such as germanium, that do not support SPs.

Subsequent studies indicate that the transmission resonances observed in the EOT phenomenon were the result of a dynamical diffraction process [14] and diffraction of evanescent waves [15]. It has been shown that in certain cases, SPs can have a negative effect on transmission [16]. These studies show that although SPs may influence the EOT phenomenon, they are not essentially causal to it.

The shape of the nano-holes makes them strongly sensitive to polarization of light [17]. The orientation of ellipses in the lattice also affects the polarization of transmission [18]. The shape also influences the position of the resonances [19, 20]. Elliptical holes with greater ellipticity display greater polarization selectivity [17]. Studies on isolated rectangular apertures showed that the cut-off wavelength and normalized transmission increased with decrease in the shorter length [21].

The sub-wavelength properties of nano-hole arrays can be used in several applications such as sensing and spectroscopy. SPR sensors can be used to sense sub-monolayer amounts of molecules [22]. Nano-hole arrays are also ideal substrates for SERS and SHG which relies on local field enhancements [12].

2.3 Effect of nano-hole shape

2.3.2 Elliptical nano-holes

The aspect ratio of nano-holes affects both the transmitted intensity and the polarization[17]. Figure 2.3 shows the transmission for x and y polarization. X-polarization was defined parallel to the (0,1) resonance direction of the array, which is perpendicular to the major axis of the array. A clear reduction in the peak of the transmission spectrum was observed when the polarization was changed form x to y polarization.

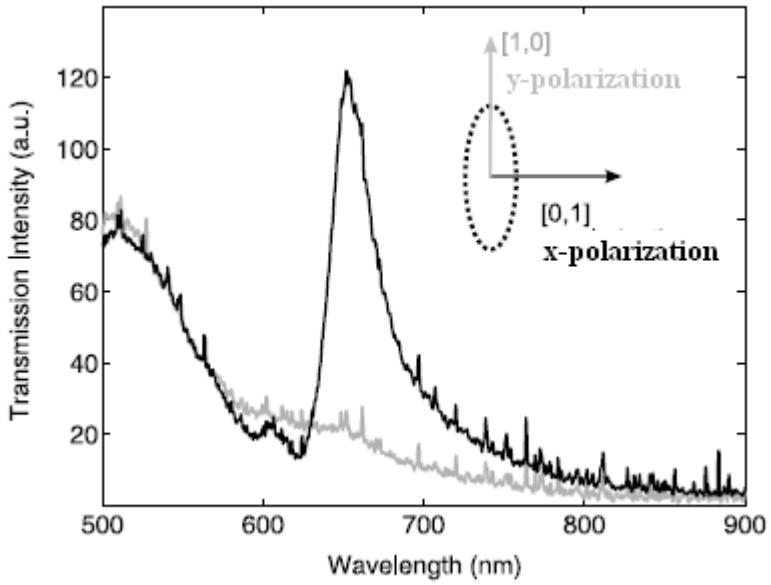

Figure 2.3: Intensity of light transmitted through elliptical nano-holes of aspect ratio 0.3. x-polarization is perpendicular to the major axis of the ellipses, and parallel to the (0,1) resonance of the array[17].

The orientation of the elliptical nano-holes was rotated relative to the lattice, and the transmission spectra of light polarized linearly along several directions between x- and y-polarizations were measured. It was found that the orientation of the electric field polarization corresponding to the peak in transmission follows the orientation of the ellipse. This is partly because the SP modes propagate parallel to the electric field polarization[4], and the Bragg resonance from the array is aligned with the optical polarization. Thus, the transmission was enhanced for polarization that is parallel to the direction in which the ellipse orientation allows for enhancement of SP mode coupling.

While it is clear that the shape of the nano-hole influences its characteristics, it is not the only factor playing a role. The orientation of nano-holes in the array also plays an important role in determining the array's characteristics[18].

Figure 2.4 shows experimental and calculated results to separate the effects of basis and lattice contributions. Figure 2.4(a) shows scanning electron microscope (SEM) images of arrays of elliptical holes and double holes. Figure 2.4(b) shows the variation of

the (0,1) transmission peak, and polarization angle with basis rotation. Figure 2.4(c) shows the variation peak transmission and polarization angle with basis rotation as computed with FDTD simulations.

Elliptical nano-holes exhibit maximum transmission when the light is polarized perpendicular to their major axis. On rotation of the basis, the corresponding polarization angle followed the rotation of the basis, and not the lattice. Whereas, for the double holes, maximum transmission for all angles was observed when polarized parallel to the (1,0) lattice direction. The polarization in this case, followed the lattice and not the basis.

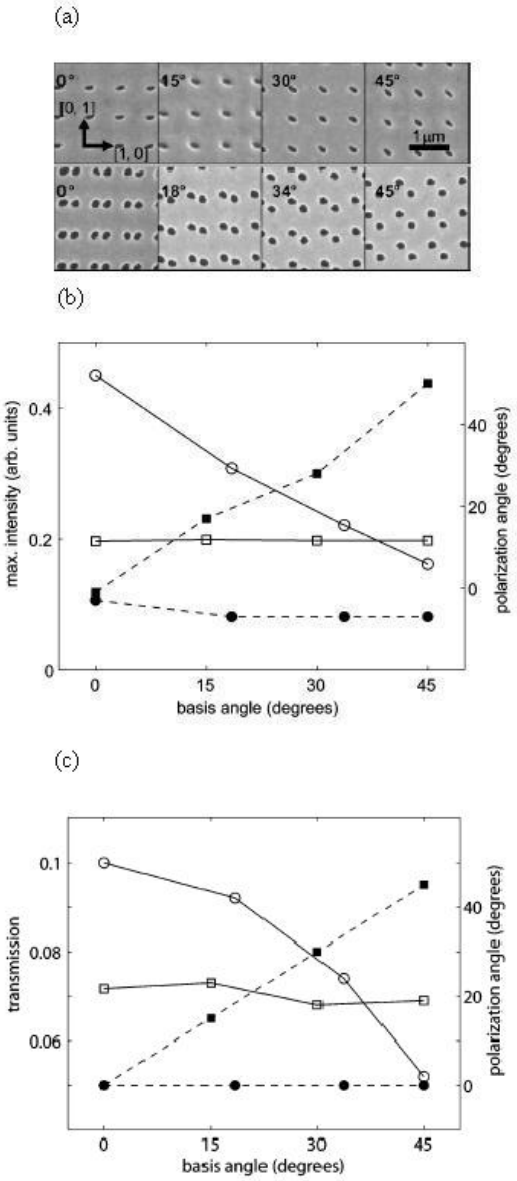

Figure 2.4: Effects of basis and lattice orientation changes. (a) Scanning electron micrographs of arrays of elliptical and circular holes with varying basis orientations within the array. Lattice directions are defined. (b) Maximum transmission intensity and polarization angle for ellipses and double holes. (c) FDTD computed transmission and polarization angle. Solid lines depict transmission intensity for ellipses (open squares) and double holes (open circles). Dashed lines show polarization angle for ellipses (filled squares) and double holes (filled circles)[18].

2.3.2 Rectangular holes

The aspect ratio of rectangular holes strongly influences the optical properties of the hole[19-21]. The works of van der Molen and Koerkamp experimentally studied arrays of rectangular nano-holes to show that increasing the aspect ratio increased the cut-off wavelength for a rectangular hole. Degiron observed the same for modes of an isolated rectangular aperture[21].

For a rectangular waveguide made of a perfect electric conductor (PEC), the electric field penetration into the metal is expected to be zero. The cut-off wavelength of the lowest order mode is given by:

$$\lambda = 2l \qquad (2.5)$$

Where l is the length of the long edge of the rectangle.

Numerical studies and rigorous electromagnetic computations on a waveguide mode of a single rectangular aperture indicated that the observed increase in cut-off wavelength occurs due to two contributing mechanisms: penetration of electric field into the metal, and coupling of SP modes into the top and bottom edges of the hole [23].

Penetration of electric field into the metal allows for longer wavelengths inside the hole, thereby increasing the cut-off wavelength. The cut-off wavelength for a rectangular aperture in a real metal is given by[21]:

$$\lambda_{cut-off} = \frac{\pi l \sqrt{\varepsilon_d}}{\arctan \sqrt{-\varepsilon_m / \varepsilon_d}} \qquad (2.6)$$

At 750nm, the real part of the dielectric constant for silver is -27.8, which leads to a 14% increase in cut-off wavelength for a 270nm hole.

The coupling of SPs into the top and bottom edges inside the hole leads to an increased effective index.

Figure 2.5 shows the effective index squared calculated for the TE_{01} mode using the effective index technique and FDTD simulations, for rectangle of various aspect ratios, as indicated in the legend. Calculations were performed for hole widths down to 15 nm where cut-off wavelengths increased up to 1260 nm.

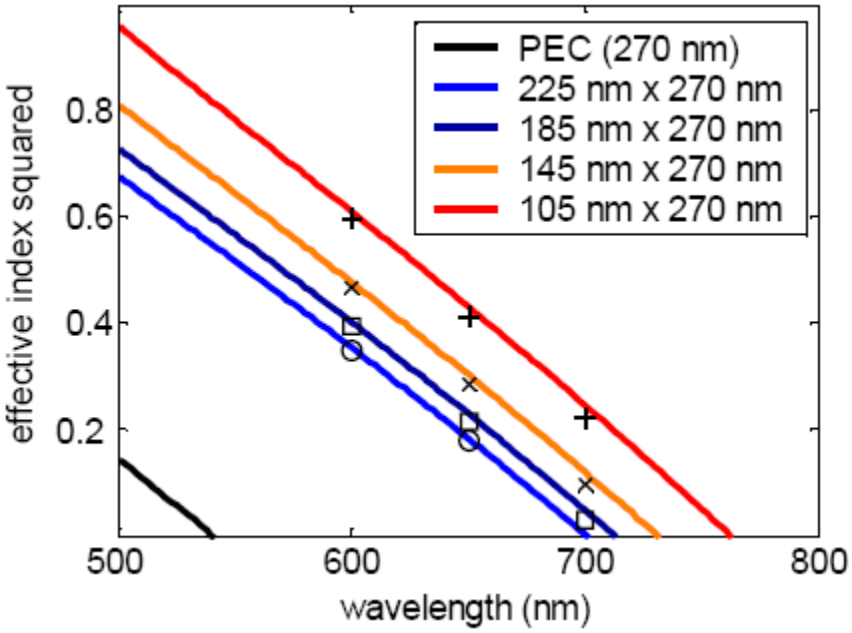

Figure 2.5: Effective index squared for TE_{01} mode in rectangular holes in real metal and a PEC computed using the effective index technique (curves) and rigorous electromagnetic computations (points) [23].

It has also been found that there exists a Fabry-Pérot resonance that leads to a maximum in transmission close to cut-off wavelength [23, 24]. In a rectangular waveguide, there is an impedance mismatch between the modes in the waveguide and free space mode. This impedance mismatch causes reflections. For a PEC waveguide, there is a negative phase shift associated with this reflection, which is given as [25, 26]:

$$\Gamma = |r|\exp(j\varphi) = 0.25\exp(j0.42\pi). \qquad (2.7)$$

For a rectangular nano-hole in a real metal, due to the presence of SPs, the amplitude of the reflection coefficient is larger than expected. Therefore, the zeroth order FP resonance exists for film thicknesses smaller than half the wavelength of light.

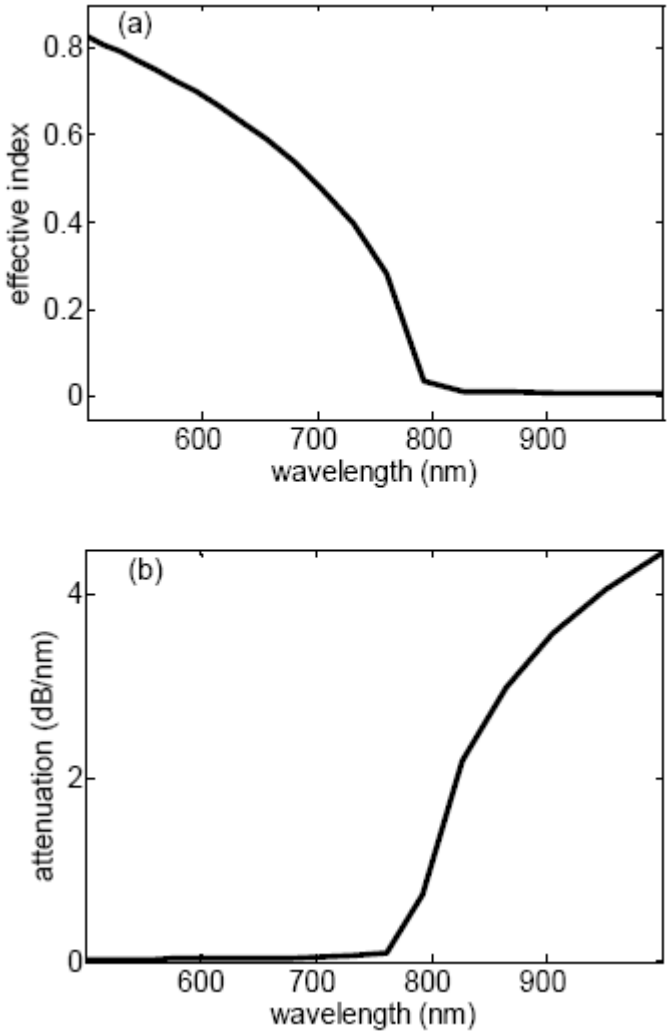

Figure 2.6: (a) Plot of effective index as a function of wavelength. (b) Loss in the film as a function of wavelength. Graphs are for a 270nm by 105nm hole in silver [24].

Figure 2.6 shows a plot of effective index and attenuation for a 270 nm x105 nm hole in a silver film, with the dielectric constants of silver calculated using the Drude model [27]. Figure 2.6(a) shows the effective index varying with wavelength, and also the fact that it reduces close to zero at the cut-off wavelength of 792nm. It does not, however, actually become zero. This is due to the finite loss of the film. Figure 2.6(b) shows the

loss of the lowest order mode as a function of wavelength. Large attenuation is observed beyond cut-off wavelength.

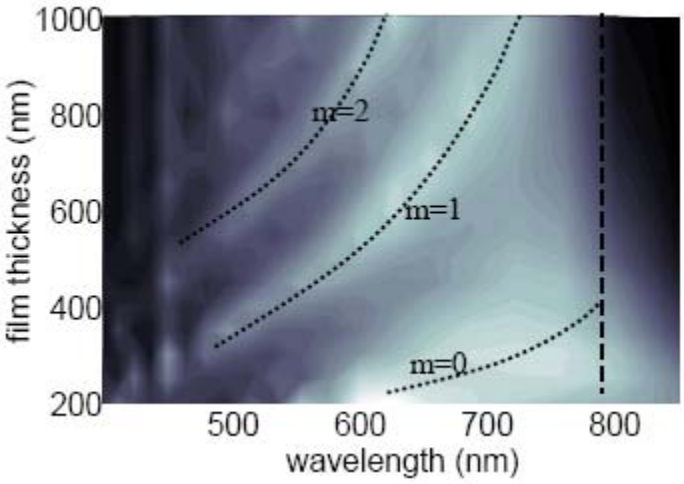

Figure 2.7: Contour plot of transmission as a function of wavelength. The cut-off wavelength, as calculated from Figure 2.6 is marked with a dashed line. Mode orders are marked m=0,1 and 2[24].

Figure 2.7 shows a contour plot of transmission through the hole as a function of wavelength. The zeroth, first and second order FP resonances are shown as peaks in transmission. The zeroth order mode is found to exist at longer wavelengths, and for very thin films due to the negative phase of the reflection between the modes in the hole and free space.

The phase of reflection of the first order mode is calculated as [24]:

$$m\pi - \left(\frac{2\pi \eta_{eff} L}{\lambda} \right) = \varphi \qquad (2.8)$$

Where η_{eff} is the effective index obtained from a modal analysis of the structure represented in Figure 2.6(a). The phase shifts so calculated were found to increase with wavelength as silver becomes a better conductor, approaching the PEC case. The resonances in the case of an isolated aperture correspond to the localized SPR (LSPR).

2.4 Nano-holes for sub-wavelength focusing

Sub-wavelength hole arrays can enhance the optical transmission, and by changing the shape and orientation of the nano-holes it is possible to tailor their optical properties. Many applications require local field enhancements, rather than increased transmission. These applications include SERS, SHG and other forms of nonlinear optics. The overlapping double hole structure has been shown to be able to provide very high local field enhancements required for many spectroscopic applications[28, 29]. The apex formed at the point of overlap of two circular holes is analogous to the gap formed in bowtie antennae [30] and optical antennae[31], which have also demonstrated strong local field enhancements.

To characterize the properties of the double-hole apex structure, FDTD simulations of the double-hole with different center-to-center spacings were performed. The diameters of the holes were fixed at 200 nm, and six different separations of 0 nm, 90 nm, 130 nm, 190 nm and 250 nm were simulated. The case with 0 nm separation represents a single circular hole, and the 250 nm separation represents a pair of isolated holes. With all other separations, different apex gaps were formed[28].

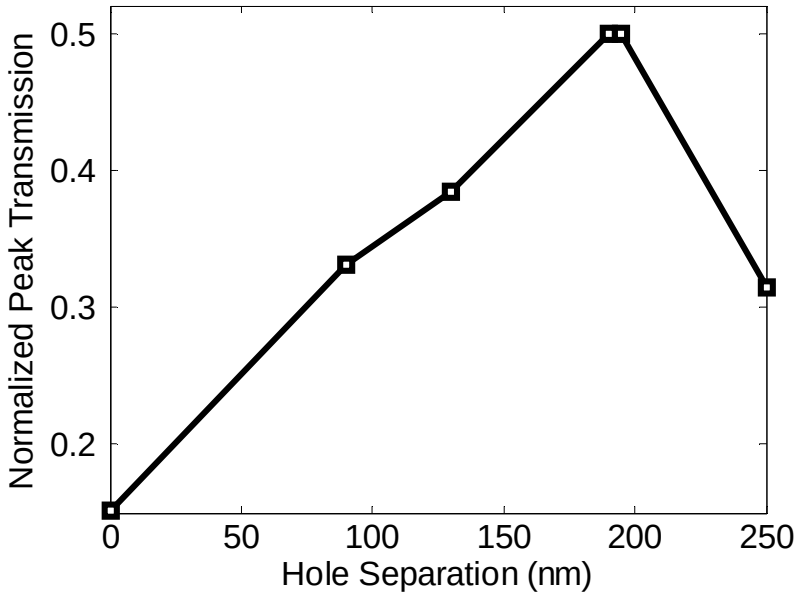

Figure 2.8: Variation of peak transmission with changes in the center-to-center spacing as calculated using FDTD simulations [28].

Figure 2.8 shows the variation of peak transmission intensity with changes in the center-to-center spacing. Maximum transmission was seen for a separation of 190 nm which corresponded to an apex gap of 65 nm. The cases where the holes were either completely isolated, or merged to form a single hole yielded results similar to past works [6, 18]. The structures with apexes exhibited a different behaviour. Higher transmission was seen in these structures. The highest transmission was seen for a center-to-center separation of 190 nm. This corresponded to an apex gap of 65 nm.

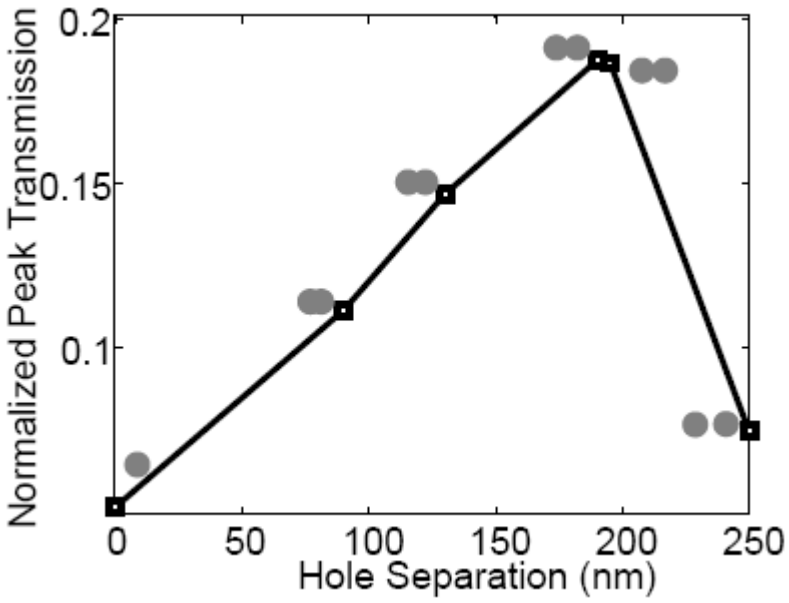

Figure 2.9: Measured peak transmission for different hole center-to-center separations [28].

Transmission measurements performed on fabricated double-hole structures with similar separations as used in the simulations exhibited characteristics that agreed well with the simulation results. Figure 2.9 shows the normalized peak transmission for different separations. The maximum transmission was seen for 190 nm separation [28]. A red shift was also observed in the transmission spectra with this separation. Although the measured transmission was significantly lower due to imperfections in the fabricated structures, such as blunter apexes, the trend observed agrees well with theory.

In addition to having significantly higher transmission than single circular holes, the double-hole structure leads to high local field intensities in the apex gap [29]. The local field intensity is important to applications like SHG because the SHG intensity varies as the square of the field intensity.

SHG is not usually observed for centro-symmetric structures like bulk gold. For structures with a broken symmetry, and rough surfaces, enhanced SHG has been observed [32]. The presence of sharp apex points in the double-hole structure thus leads to enhanced field intensities, and thus enhanced SHG.

SHG measurements were performed on a number of double-hole arrays with different center-to-center separations, varying from a single hole (separation of 90 nm) and two isolated holes (separation of 250 nm). The sharpest apex was formed for the array with a center-to-center separation of 220 nm.

The SHG intensity was found to depend strongly on polarization and the hole spacing [29]. Figure 2.10 shows the variation of SHG intensity with spacing for two different polarizations. X polarization was defined parallel to the major axis of the double-hole structure, and y polarization was defined perpendicular to it, or aligned with the apexes. A strong peak is seen in the SHG intensity for a hole spacing of 220 nm and y polarization. This is almost 10 times the intensity for the 90 nm separation. Linear transmission measurements showed a corresponding enhancement of 1.5 times. Considering the squared dependence of SHG signal, this should correspond to an enhancement of 2.25 times. However, an additional enhancement of 4.44 times was observed.

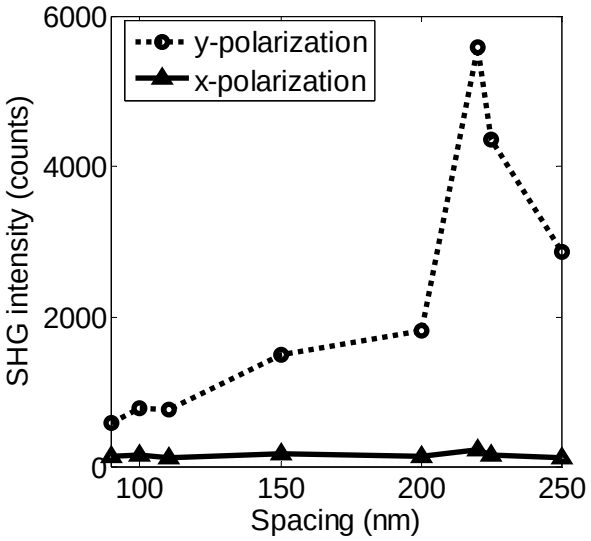

Figure 2.10: SHG intensity for x and y polarized input for different hole separations [29].

Figure 2.11 shows the y polarized field intensity near the apexes computed using FDTD calculations for the hole separation of 220 nm [29]. The fields are calculated 5 nm

above the sample surface. The field near the apexes increases by 4 times. This translates to a 16 times enhancement in SHG signal.

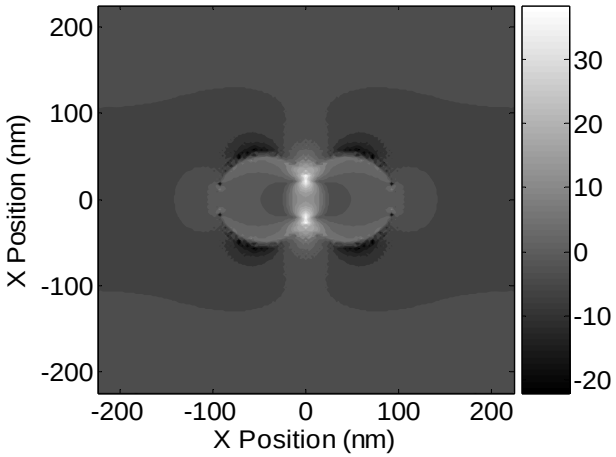

Figure 2.11: y polarized field intensity for hole separation of 220 nm computed using FDTD simulations [29].

These findings indicate that the presence of sharp apexes can enhance local field intensity. This makes the overlapping double-hole structure useful for non-linear applications.

2.5 Nano-hole arrays in spectroscopy

Enhanced spectroscopic methods, such as SERS and SEFS, are very useful in chemical analysis. These methods allow the detection of extremely small amounts of adsorbed species, even achieving the ultimate sensitivity at the single molecule level [33]. The enhancement in the field intensity resulting from sub-wavelength apertures can be tailored by optimizing their fabrication parameters, such as shape, film thickness and periodicity. Periodic arrays of nano-holes have been shown to be good substrates for surface enhanced spectroscopic techniques such as SERS [34] and surface enhanced fluorescence [35].

For SERS measurements using the nano-hole arrays, a probe dye molecule was adsorbed onto the array of nano-holes and the excitation laser was directed through the back of the substrate. Therefore, the excitation laser needed to go through the nano-holes to excite the molecules adsorbed on the gold surface and the scattering was measured in a forward geometry [34].

Figure 2.12 shows the enhanced Raman spectra from three nano-hole arrays of different periodicities fabricated on a gold film coated with 10 μM of oxazine 720 dye in methanol. The enhancement is seen to depend upon the periodicity. The maximum enhancement was seen from the array with periodicity 560 nm. At excitation wavelength, this array exhibited maximum transmission.

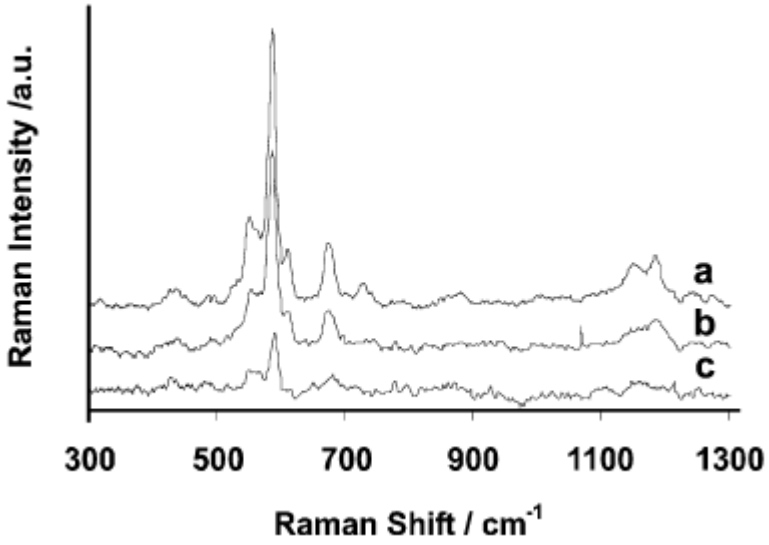

Figure 2.12: SERS signal from arrays of periodicity (a)560 nm, (b) 590 nm and (c)620 nm. The spectra are offset for clarity [34].

For this experimental geometry, when the laser wavelength coincides with the surface plasmon resonance, enhanced transmission for normal incidence is observed. Hence, an increase in the number of laser photons reaching the gold-air interface is expected under resonance conditions. This allows for an enhanced field at the surface. The enhanced local field is required for any surface-enhanced spectroscopic method. Therefore, the strongest Raman signal is expected for the array that has enhanced transmission closest to the laser wavelength. This is in agreement with the experimental results.

The enhanced transmission and local field intensity of sub-wavelength apertures in a metal film can be used to excite a fluorescent material adsorbed on the surface. Higher fluorescence sensitivities are achieved when fluorescence spectroscopy measurements are performed on sub-wavelength hole arrays [35]. Several nano-hole arrays with different periodicities were spin-coated with polystyrene (PS) doped with varying concentrations of Oxazine 720 fluorescent dye. The excitation laser was directed at the back of the substrate and the extraordinary transmission of light through the nano-holes led to the dye being excited. Enhanced fluorescence, and consequently, high fluorescence sensitivities were observed at SPR conditions.

Figure 2.13 shows the measured fluorescence enhancement as a function of periodicity. Seven different square arrays of circular holes with 100nm diameter and different periodicities were fabricated. The fluorescence spectra obtained indicated quite clearly that the fluorescence efficiency was array dependant. The highest fluorescence intensity was obtained for the 553nm array, which was the array that exhibited maximum enhanced transmission at the laser wavelength. The enhancement factor was found be 82.

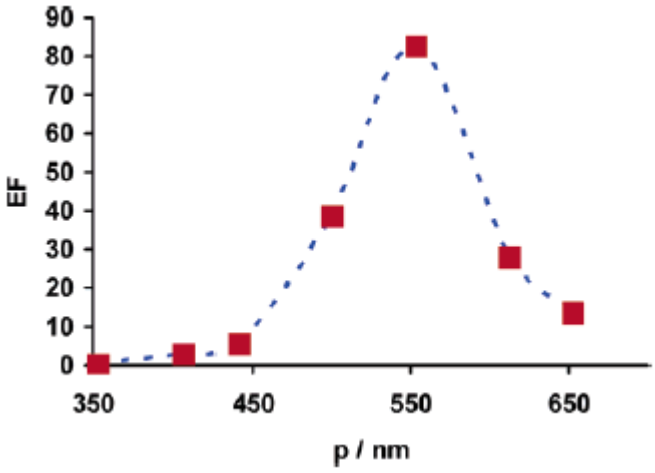

Figure 2.13: Enhancement factor in the fluorescence for arrays with different periodicities. Arrays were spin coated with a PS film dopes with 9.6 μM of Oxazine 720 [35].

A non-linear relation was found to exist between the transmission and integrated fluorescence. This was attributed to secondary enhancements due to Oxazine emission [35].

2.6 SPR sensors based on nano-holes arrays

Most SPR sensors that are commercially available operate based on total internal reflection using what is known as the Kretschmann configuration [36]. Here, SPR is excited via prism coupling. The excitation is beamed onto the metal film by means of a prism of high refractive index. On the other side of the metal film is the analyte medium. The dispersion in this case depends on all the three media. Based on the analyte used, the reflection spectrum will shift. The dip in the reflection spectrum corresponds to the SPR of the ensemble of media.

The SPR sensor based on arrays of nano-holes operates based on transmission rather than reflection [37]. This is useful because the transmitted and measured signals are collinear. The setup is therefore easier to align. Also, when nano-holes are used for sensor applications, the resulting localization of the analyte can directly benefit from the local field intensities and optical properties of nano-holes, thus making nano-hole sensors useful.

A sensor based on arrays of nano-holes on a gold film was used to monitor binding of organic and biological molecules [37]. Several arrays of different periodicities with hole diameter of 200nm were fabricated. The slides were immersed in a 1mM ethanoic solution of 11-mercaptoundecanoic acid (MUA) for a period of 24 hours. The surface was then dried, and the normal transmission spectra were measured. The surface was then further modified by bovine serum albumin (BSA) which adsorbed on top of the MUA monolayer.

Figure 2.14 shows the normalized transmission spectra of normally incident white light though one of the arrays of nano-holes. The transmission spectrum through the array of nano-holes prior to the surface modifications shows a sharp resonance at 645nm. After surface treatment with MUA, the same array showed a shift in maximum transmission to 650nm. An additional shift to 654nm was observed after the BSA protein was adsorbed on the MUA surface.

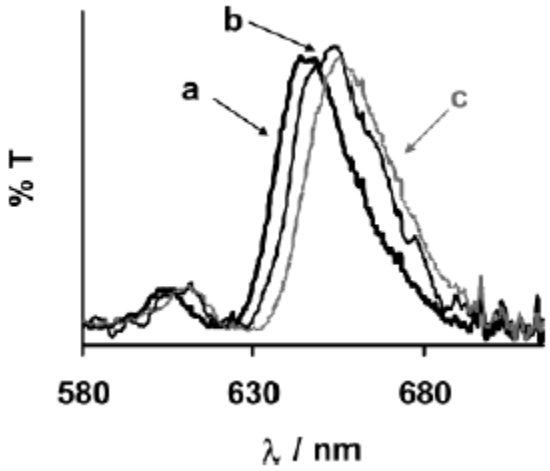

Figure 2.14: White light transmission spectra through the nano-hole array for (a) clean gold surface (b) gold treated with MUA and (c) gold-MUA surface with adsorbed protein [37].

Microfluidic devices enable the manipulation of the small quantities of chemicals generally used in biomedical analyses. So-called lab-on-chip or micro total analysis systems promise increased quality and quantity of analytical tests, with decreased time and cost requirements [38].

Sensors based on the nano-hole arrays have been integrated into microfluidic devices to form efficient sensing devices [39]. Figure 2.15 shows a schematic representation of the SPR sensor chip. A number of nano-hole arrays, 20μm by 20μm, with hole diameter 100nm and different periodicities were fabricated on a gold film. Microfluidic channels were constructed by soft lithographic methods, and aligned over the sensor array substrate. The two microfluidic configurations enabled single solution experiments over

multiple arrays as well as the generation of concentration gradients across a set of similar arrays. Glucose solutions of known refractive index were used to determine the sensitivity, 333nm/ RIU (refractive index unit). Employing the set of nanohole arrays, the device was applied to detect microfluidic concentration gradients as well as surface binding during the assembly of cysteamine monolayer-biotin-streptavidin surface groups.

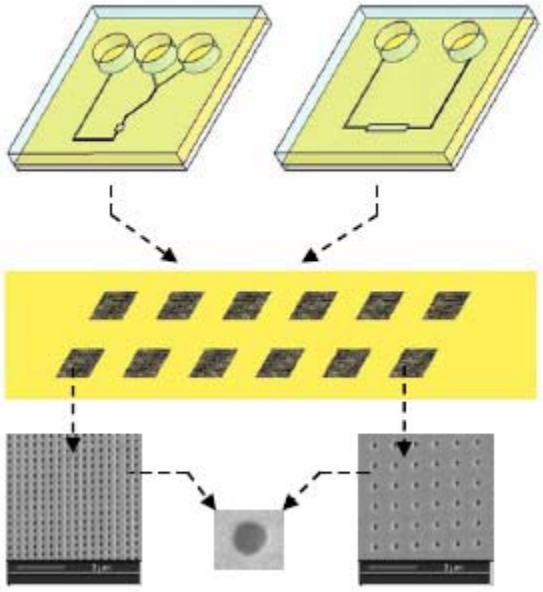

Figure 2.15: Schematic representation of nano-hole arrays used in microfluidic sensor chip [39].

Multiple arrays of nanoholes, differentiated by periodicity, may be integrated and used as SPR chemical/biological detectors in a microfluidic chip format. Combining the unique optical properties of nano-hole arrays with microfluidic processing and control presents several opportunities in bio-sensing.

Double hole arrays have also been implemented in real-time biosensors, to detect the formation of a self assembled mono-layer of 11-amoni-1-undecanethiol hydrochloride, and adsorption of protein on the surface [40].

Although sensors operating on transmission are easier to align and implement, sensors operating based on the Kretschmann configuration are known to be more sensitive.

2.7 Motivation behind PBRs

The transmission of light through an isolated sub-wavelength aperture in a metal film was observed to be enhanced with the introduction of appropriate surface structures [41-44]. The enhancement from these surface structures came about from resonant modes being set up between the hole and the surface structures. Such enhancements were seen in from single holes surrounded by periodic square and circular dimples [43], and from sub-wavelength slits flanked by periodic gratings [41, 42, 44].

The surface structures performed two funstions: enhancing the transmission through the aperture, and improving the beaming angle [41, 42, 44]. The enhancement in transmission arises due to resonance of modes between the surface structures and the aperture. The position of the resonances is determined by the geometry i.e. the periodicity of the surface structures. The low beaming angle obtained on the exit side is due to the scattering of SPs and subsequent re-emission by the surface structures surrounding the aperture. In the absence of the corrugations, a large beam divergence angle was observed.

In a metal film with periodic arrays of nano-holes, near field studies exhibit scattering of SPs off the edge of the nano-hole array excited by a coherent light source [45]. The scattered SPs were seen to have coherent propagation distances of tens of microns. This scattering and propagation of SPs constitutes a loss mechanisms because the SPs that must contribute to the EOT through the array scatters away. Further, in the context of a densely integrated plasmonic device, this scattering represents corss talk, which could be detrimental to the functioning of the device.

The PBR structure is proposed to minimize this loss: it consists of periodic surface corrugations which have a periodicity equal to half the array's periodicity. Thus, the structures fulfill the Bragg reflection condition, and when optimally desgned, can enhance EOT through the array by recapturing scattered SPs.

2.8 Motivation behing quasiperiodic nano-hole arrays

The EOT phenomenon through nano-hole arrays has long been thought to rely on the periodicity and translational symmetry of the array. Quasiperiodic structures do not exhibit any translational symmetry, but display other interesting symmetries. Quasiperiodic arrays of sub-wavelength apertures in metal films have been shown to exhibit enhanced transmission [46, 47]. Arrays of quasiperiodic nano-holes also show formation of tightly focused hot-spots of light, which has a lot of potential in spectroscopic and sensing applications [48]. Two-dimensional dielectric quasicrystals have been shown to exhibit bandgaps for both TE and TM polarizations [49], which is contrary to belief that a regular periodic lattice is fundamentally important to the existance of a bandgap.

In order to explore the properties of plasmonic quasicrystals, quasiperiodic arrays of nano-holes in a gold film are studied. The unique rotationally symmateric diffraction pattern is analyzed. In order to better understand the physics of the quasicrystal, FDTD calculations are performed of the quasicrystal structure.

2.9 Conclusions

In this chapter, past works on EOT from nano-hole arrays were discussed. The origin of the EOT, and some important effects of the SPR phenomenon were presented. Some important applications of nano-hole arrays in spectroscopy and sensing were discussed.

Chapter 3

Fabrication

Introduction

This chapter describes the fabrication of the nanostructures studied in this research. Section 3.1 describes the focused ion beam (FIB) milling process. Section 3.2 describes the fabrication procedures and parameters for fabrication of nano-hole arrays using FIB. Section 3.3 describes the creation of stream files used to control the CAD interface of the FIB. Section 3.4 outlines the fabrication of the PBR structure. Section 3.5 describes the fabrication of the quasicrystal nano-hole array structure.

3.1 Scanning Electron Microscopy and Focused Ion Beam milling

Scanning electron microscopy is a versatile technique used for non-destructive topographical analyses of materials' surfaces at the nano-scale. In its simplest form, a scanning electron microscope consists of a metal electron source. The source is made to emit electrons either under high temperatures (thermionic emission) or extremely high fields (field emission). The most commonly used electron source is a Tungsten filament because of its high melting point and low vapour pressure. Once electrons are emitted, they are deflected by one or more sets of condenser coils to scan the surface of the sample in a raster fashion. Secondary electrons are emitted from the sample when electrons impinge on it. These secondary electrons are collected by a detector, amplified and the signal digitally reconstructed to form an image of the sample's surface.

Focused ion beam milling is a mask-less lithography technique commonly used for the fabrication of micro and nano-scale structures. The working of a FIB is similar to the

working of a SEM. The source in a FIB is a liquid metal ion source (LMIS) in a reservoir attached to a Tungsten needle. The liquid metal flows to the tip of the needle where ion emission is achieved by high voltages applied to the electrodes. The emitted ions are then focused similar to electrons in a SEM. When the high energy ion strikes the sample, etching of the substrate material is achieved. Most FIB systems in use allow for in-situ fabrication and imaging using FIB and SEM respectively.

The focus and astigmatism correction are important aspects of using the SEM and FIB. Proper focusing is important to any imaging technique. Astigmatism is the uneven spread of the spot due to imbalanced focusing fields. The result of astigmatism is an elliptical spot rather than a circular one. SEM images appear distorted as a result of beam astigmatism. Astigmatism in FIB will lead to imperfections in the shape of the milled structures, for example a circular hole will be milled as an elliptical hole.

3.2 Fabrication parameters

Accurate control of the etch pattern, etch depth etc can be achieved with the FIB. Various parameters controlling the FIB are the accelerating voltage, beam current, magnification and beam dwell time. All milling done in this research was carried out at an accelerating voltage of 30kV and a magnification of 5000×. At this magnification, the spot size of the FIB was 7.14 nm. This was measured by calibrating the FIB spot size. Using the tools in the CAD interface, a spot corresponding to a single pixel was milled at 5000×. Subsequently, an SEM image of the milled pixel is taken, and using the measurement tools in the interface, the size of the spot was determined.

The etch depth is controlled primarily by beam current and beam dwell time. The beam current dictates the intensity of the ion beam, and can be set from a menu in the FIB interface, as can the accelerating voltage and magnification. The beam dwell time is simply the amount of time the ion beam scans a particular pixel. The longer the beam

scans a pixel, the more material gets etched away. Figure 3.1 shows the differences in etch depth obtained by different beam dwell times

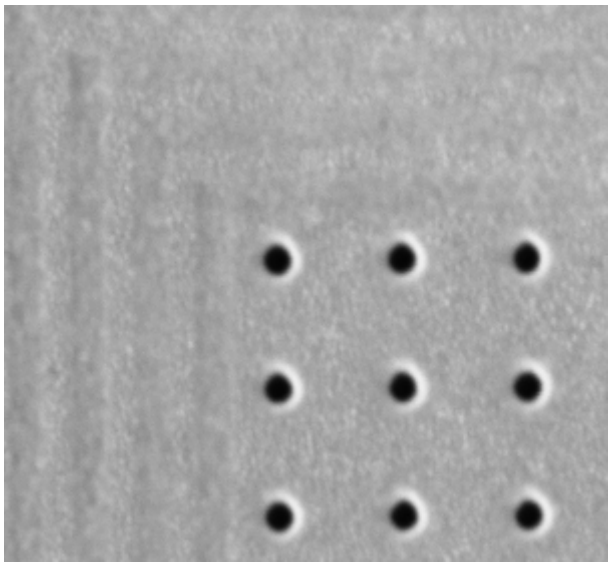

Figure 3.1: SEM of nano-hole array flanked by partially milled gratings. Difference in etch depth is achieved using different dwell times, seen as the difference in depth between the holes and gratings.

3.3 Stream files

The CAD interface of the FIB system allows accurate control of the pattern etched. Most commonly, this is done in two ways. A bitmap image of the pattern to be etched can be fed into the interface along with beam current and dwell time. The CAD interface then translates this bitmap into pixel coordinates to be milled, based on the greyscale.

Another method of pattern definition is through stream files. A stream file is essentially a series of pixel coordinates compiled into a data file along with the beam dwell time in ns. When fed into the interface, the stream file dictates the x and y coordinates to be scanned by the ion beam. At a magnification of 5000×, the field of view consists of

4096×4096 pixels, and each pixel corresponds to 7.14 nm. A stream file can be produced by a script file which can be programmed to read an input file containing the dimensions of the structure, the periodicity and required dwell times. The script can then generate a 4096×4096 matrix that holds values of either 0 or the required dwell time for that position. The coordinates of the matrix elements that are greater than zero can then be extracted and fed into stream file along with the beam dwell time.

The stream file is typically organized as follows:

- 's'- This is the first character in the stream file. This character indicates that a stream file follows
- Loop: This number indicates the number of times the stream file has to be looped.
- Count: This is the total number of pixels that have to be milled. This number has an upper limit of one million.
- Beam dwell time X coordinate Y coordinate: These are specified for every pixel to be milled.

The parts of a typical stream file are presented in Appendix A.

In order to etch completely through the sample, one of two different methods can be adopted. The ion beam current and dwell time can be increased until the sample is etched all the way through. Alternately, the beam dwell time and the number of loops can be changed. This option is usually preferable because a very high beam current can lead to a larger spot than acceptable, leading to large levels of dimensional distortion. The number of loops is determined after a number of calibration runs.

Whether the sample has been etched through or not can be determined by the contrast in the SEM image, or by energy dispersive spectroscopy (EDS) analysis. When milled correctly, for a scan area covering a hole and some surrounding gold, EDS analysis will show gold, silicon and oxygen. A spot in the hole should show only silicon and oxygen, as glass is SiO_2.

The substrate used for FIB milling was a commercially available 100 nm thick gold film evaporated on a 3 mm thick glass slide. A 5 nm thick chromium film is provided for adhesion. The chromium film has previously been shown to suppress surface waves on the gold-glass interface [18].

The script files used to generate the streams for fabrication were written in Matlab. Matlab was chosen because of ease of use, portability of scripts and the capability to preview the pattern before fabrication. Figure 3.2 shows an image of the pixel matrix used to create the quasicrystal nano-hole array.

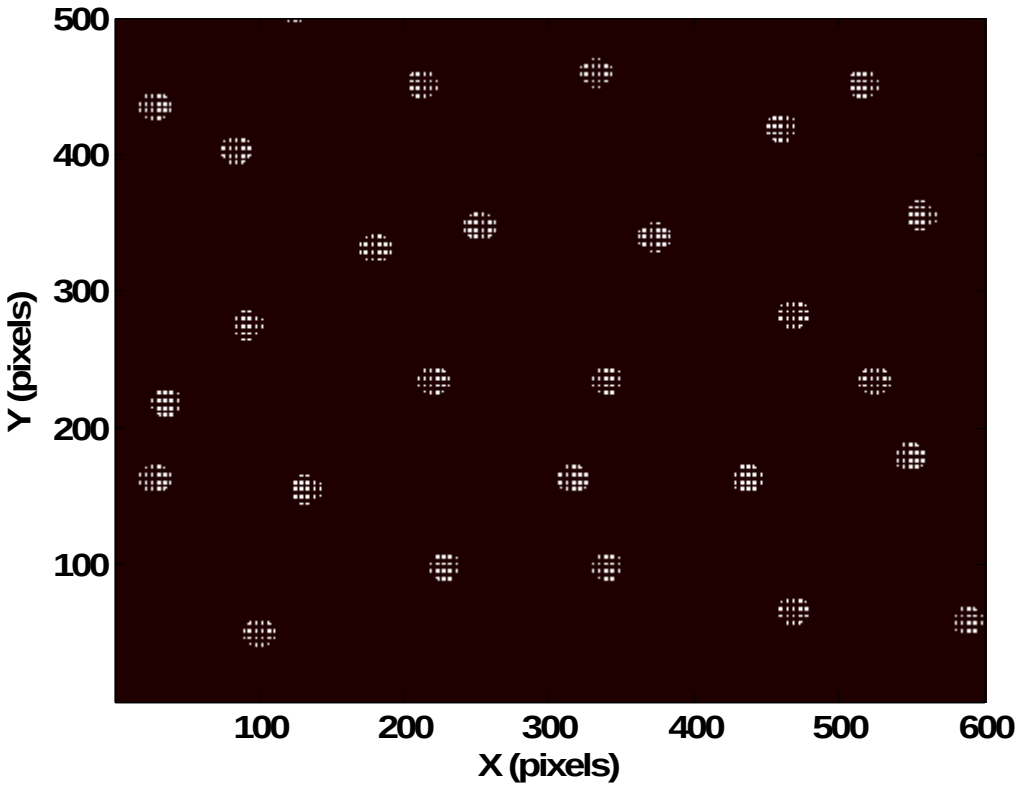

Figure 3.2: Preview of pixel matrix used to create the stream file for the quasicrystal nano-hole array.

3.4 Fabrication of plasmonic Bragg reflectors

Figure 3.3 shows scanning electron micrographs of an array of circular holes flanked by Bragg reflectors. The reflectors take the form of partially milled lines and dimples.

The PBR structure is fabricated essentially by pre-setting two different beam dwell times for the array and the reflectors. The array dwell time is set at 3000 ns in order to enable milling completely through the gold film. The dwell time is set at 50 ns for partial milling of the gold film. The reflectors take the dimensions of the holes in the array.

The reflectors are placed a half wavelength or periodicity away from the edge of the array, and have half the periodicity of the array. Other separations of the reflectors from the array, up to a wavelength, were also fabricated. Structures consisting only of the reflectors, without the hole array were fabricated to characterize their optical transmission.

Arrays of holes of diameter 150 nm with periodicity 800 nm were fabricated. The arrays were 15 μm×30 μm. The reflector layers spanned 7.5 μm×30 μm, and were placed on either side of the array.

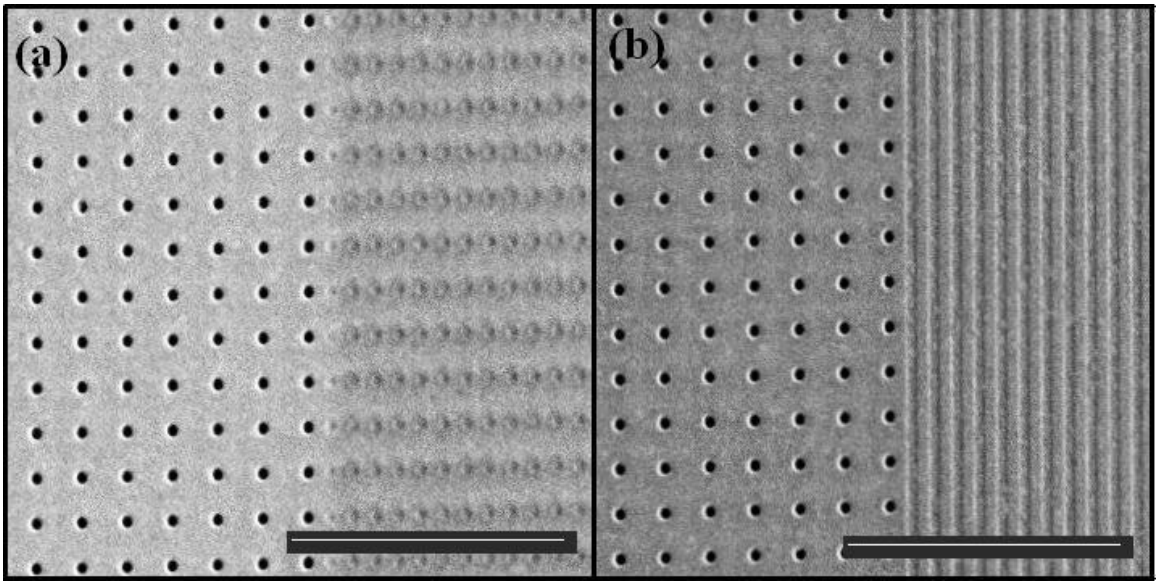

Figure 3.3: Scanning electron micrographs of nano-hole arrays flanked by (a) Dimpled PBRs and (b) line PBRs. The scale bar corresponds to 2µm.

In addition to arrays with reflectors on two sides, 15 µm×15 µm arrays flanked by reflectors on all sides were fabricated as well. Figure 3.4 shows a SEM image of a 15 µm×15 µm array of nano-holes of diameter 150 nm and periodicity 800 nm. The array is flanked by PBR layers on all four sides.

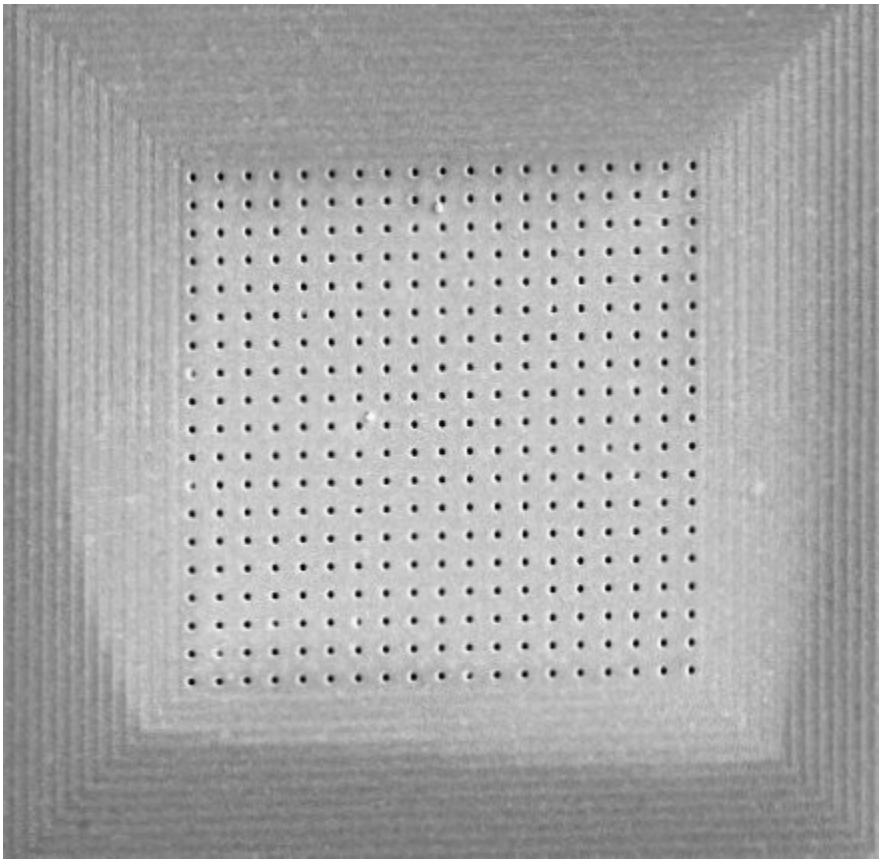

Figure 3.4: SEM of a 15 µm × 15 µm array of nano-holes of diameter 150 nm and periodicity 800 nm flanked by PBRs on four sides.

The Matlab scripts used to fabricate the PBR structures are presented in Appendix B and C.

3.5 Quasicrystal array fabrication

The quasicrystal array is based on a Penrose tiling of a plane with thick and thin rhombuses [50]. The thick rhombus has an acute angle of 72° and the thin rhombus has an acute angle of 36°. The side lengths of both rhombuses are equal. The Penrose tiling fabricated has a five-fold rotational symmetry. Figure 3.5 shows a Penrose tiling with five-fold rotational symmetry. Holes are placed at the vertices of the rhombuses.

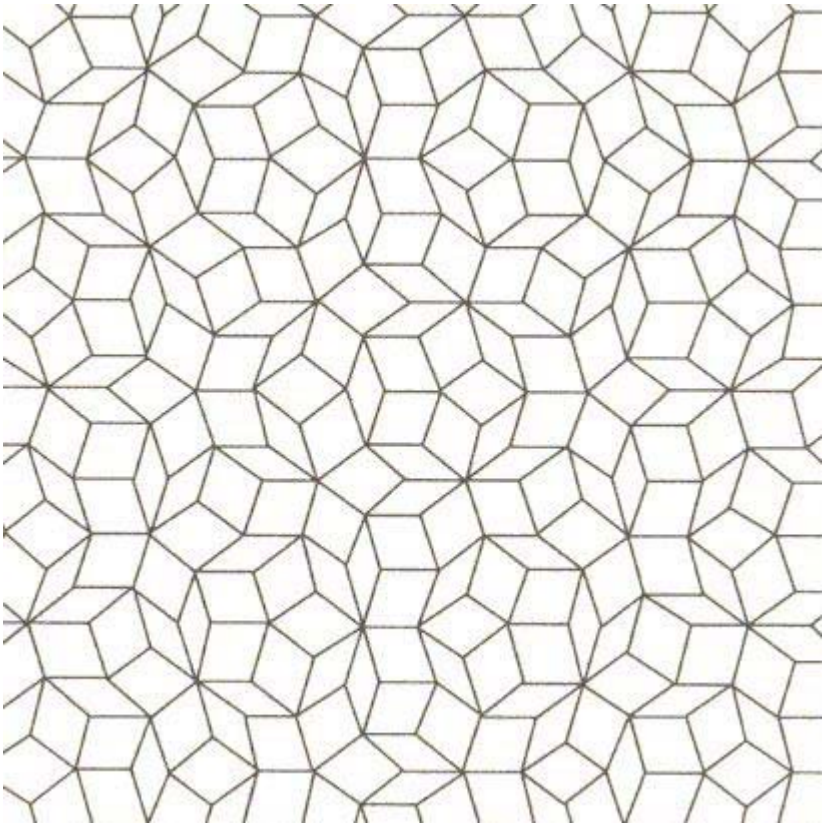

Figure 3.5: Penrose tiling with thick and thin rhombuses, with five-fold rotational symmetry[51].

The positions of the vertices were determined using the deflation technique [52]. An image file was created with the vertex points. A Matlab script was then used to load this image, and treat it as a vector of colour map data. The vector was then scaled to create matrices with positions of the centre of each hole. Stream files for milling quasicrystal nano-hole arrays with rhombus side length *d* (periodicity) of 700 nm, 800 nm and 900 nm were then generated from these matrices.

Figure 3.6 shows SEM images of a quasicrystal nano-hole array with holes of 150 nm diameter and a periodicity of 700 nm, taken at two magnifications.

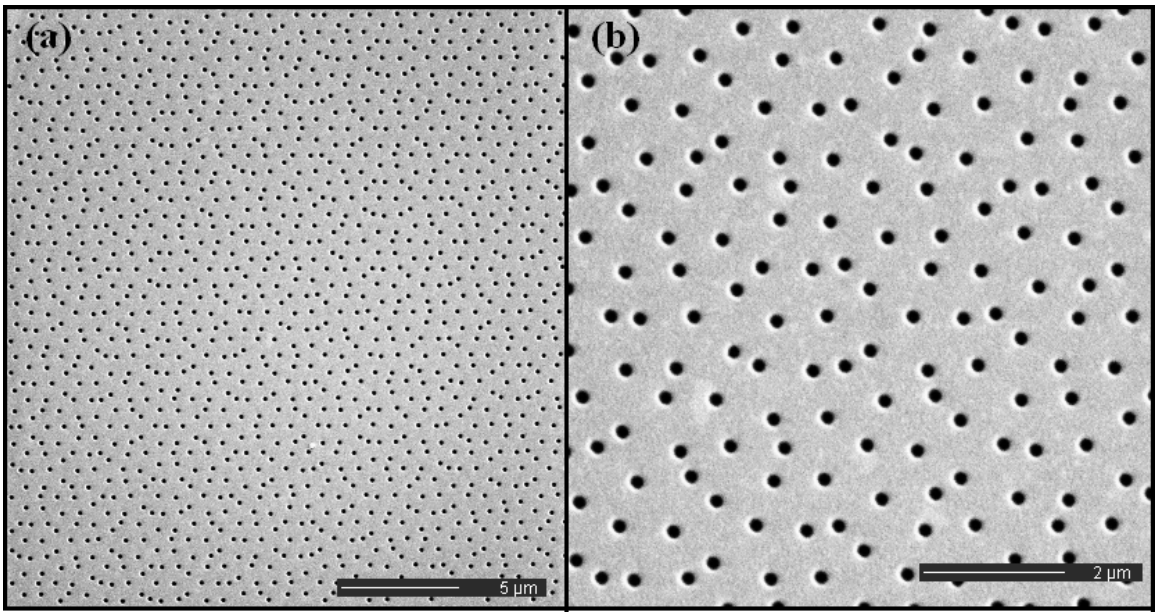

Figure 3.6: SEM images of a quasicrystal nano-hole array with holes of 150 nm diameter and a periodicity of 700 nm.

The Matlab script used to fabricate the quasicrystal structure is presented in Appendix D.

3.6 Summary

This chapter outlined the processes and methods used for fabrication of nano-hole arrays. Concepts of FIB and SEM were briefly described. Commonly used fabrication parameters were discussed. The working of stream files and the CAD interface of the FIB were outlined. Specifically, fabrication of PBR structures and quasicrystal nano-hole arrays were discussed.

Chapter 4

Transmission and diffraction experiments

Introduction

This chapter outlines the experimental methods used in this research. Section 4.1 describes the linear transmission measurements, explaining the components used. Section 4.2 outlines the setup for diffraction measurements.

4.1 Linear transmission measurements

Figure 4.1 shows a schematic representation of the experimental setup used to measure the linear transmission spectra of the nano-hole arrays. A broad-band halogen lamp is used as the illumination source. A combination of a 20× microscope objective and an iris is used to focus the incident beam to a spot of diameter 30μm.

The sample is mounted on a XYZ translation stage to allow for freedom in moving the sample. The transmission spectrum of the nano-hole array is collected by a fiber-optic coupled UV-Visible spectrometer. The spectrometer fiber is held by a XYZ translation stage which helps optimize the fiber position to collect zeroth order transmission.

A linear polarizer is used to define the polarization state of the incoming beam. Imaging of the sample and the beam spot is done using a CCD camera to ensure accurate focusing. The entire ensemble performs the function of an optical microscope.

The integration time for the spectrometer scan, number of scans to average are set on the spectrometer interface. Dark noise correction is also done on the interface.

In order to reduce noise, a function was written in Matlab to perform adjacent average smoothing of the raw spectral data with a moving window. The width of the window was

set according to the noise in the signal. A higher noise level would require a wider window for effective noise reduction. All spectra were normalized to the source spectrum.

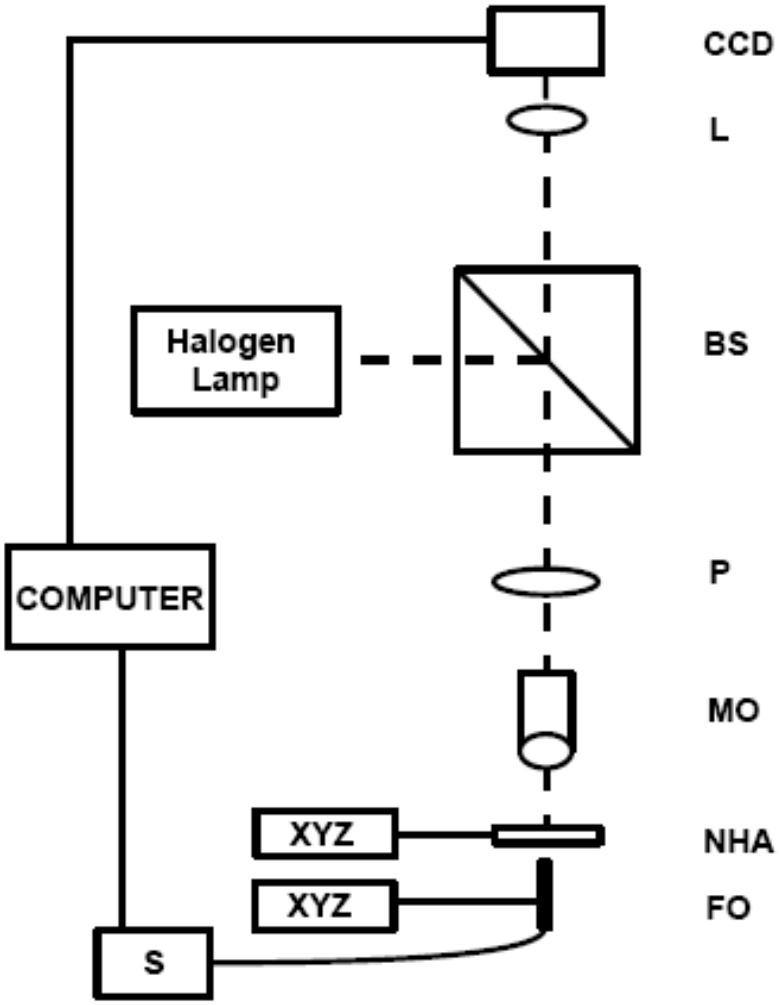

Figure 4.1: Linear transmission measurement setup. S: Spectrometer, FO: Fiber Optic, NHA: Nano-Hole Array, MO: Microscope Objective, P: Polarizer, BS: Beam Splitter, L: Lens, CCD: CCD camera.

4.2 Diffraction measurements

Figure 4.2 shows a schematic representation of the diffraction measurement setup. A He-Ne laser is the source of illumination. This is focused onto the sample using a 20× microscope objective. A linear polarizer is used to alter the polarization state of the incident beam. A CCD camera is used to image the sample, which is mounted on a XYZ translation stage. The post holding the sample can be rotated to give the sample various tilt angles allowing for non-normal incidence of the beam. The diffraction pattern is observed on a translucent screen. Images of the diffraction pattern are taken using a digital camera.

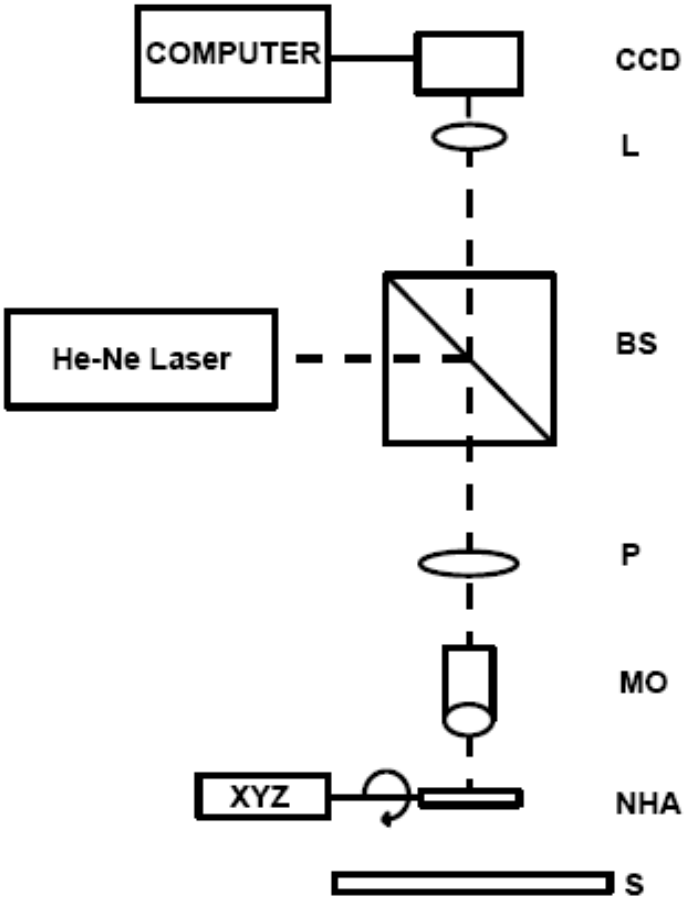

Figure 4.2: Schematic diagram of the diffraction setup. S: Screen, NHA: Nano-Hole Array, MO: Microscope Objective, P: Polarizer, BS: Beam Splitter, L: Lens, CCD: CCD camera.

4.3 Summary

Experimental setups for transmission and diffraction measurements were described. Methods for transmission spectra measurement, normalization and noise reduction were outlined.

Chapter 5

Plasmonic Bragg reflectors

Introduction

In this chapter, the experimental results and analysis of the plasmonic Bragg reflector (PBR) structure are presented. In section 5.1 the motivation behind the development of the PBR structure is presented. In section 5.2, linear transmission measurements showing enhanced EOT from arrays with PBRs. The polarization dependence of the PBR structures is studied and dimpled and line PBRs are compared. In section 5.3, arrays with PBRs placed at different separations from the array are compared. In section 5.4, linear transmission measurements of nano-hole arrays flanked by PBRs on all four sides are presented.

5.1 Motivation

Resonances observed in EOT from nano-hole arrays are dictated by the periodicity of the array [6]. SPs scattering off the edge of nano-hole arrays have coherent propagation distances of tens of microns [45]. This is useful if coupling between adjacent structures on plasmonic integrated circuits is required. If coupling is not required this constitutes unwanted cross talk. The scattering and propagation of SPs away from the array also constitutes a loss mechanism, as the SPs are a part of the EOT phenomenon.

EOT has been observed in isolated sub-wavelength holes and slits when surrounded by periodic surface corrugations [41-44]. When an isolated hole is surrounded by partially milled grooves or dimples, resonant transmission is observed, with the resonance wavelength dependent on the periodicity of the surface structures [43]. An isolated slit flanked by grooves shows both enhanced transmission [41] and improved beam directionality [42]. In these works, periodic surface structures are used to enhance the

transmission through apertures. However, the resonance wavelength is dictated by the surface structures. For an array of apertures, the resonance is dictated by the periodicity of the array. Any means to enhance EOT from an array should cause no change to the resonance wavelength.

Here, surface structures with half the array's periodicity are used to flank the array and enhance EOT. Because these structures have half the array's periodicity, they satisfy the Bragg condition, and hence the name plasmonic Bragg reflectors.

5.2 Transmission enhancement and polarization dependence of PBRs

Figure 5.1 shows the transmission spectra of the nano-hole array flanked by reflectors on two sides for horizontal polarization. Horizontal polarization is perpendicular to the orientation of the PBR layers. The array has a periodicity of 800 nm, and so has a (1,0) resonance at 870 nm and a broad (1,1) resonance at around 700 nm. These resonances arise from the gold-air interface. Resonances on the gold-glass interface are suppressed due to the lossy chromium layer [18]. Enhancement of the nano-hole array's EOT is seen with the introduction of the PBR layers with negligible change in the resonant wavelengths. With the line PBRs, there is a very small blue shift in the transmission peak at 870 nm. Considering the experimental error from noise, and systematic variations in the FIB spot size, this small blue shift, of less that 10 nm can be attributed to a difference in the reflection characteristics of the dimples and lines.

The peak transmission is measured from the minimum around 850 nm, commonly attributed to the Wood's anomaly, to the peak at 870 nm. The resonance at 870 nm is considered because although it is narrower than the (1,1) peak, it is greater than it.

The resonance at 870 nm is enhanced by nearly 2 times due to line PBRs and nearly 1.8 times due to the dimpled PBRs. For the (1,1) resonance, the dimpled PBRs show slightly lesser enhancement than the line PBRs.

The enhancement of transmission occurs because the waves reflected by the PBRs are in-phase with the surface wave propagating from the holes in the array. This leads to maximum constructive interference.

There has been no observed influence on the transmission spectrum from the illumination of the PBRs. In samples with only the PBRs, and no hole-array, no transmission was observed. The illumination of the PBR is not phased-matched in order to couple light that is incident normal to the surface towards the array.

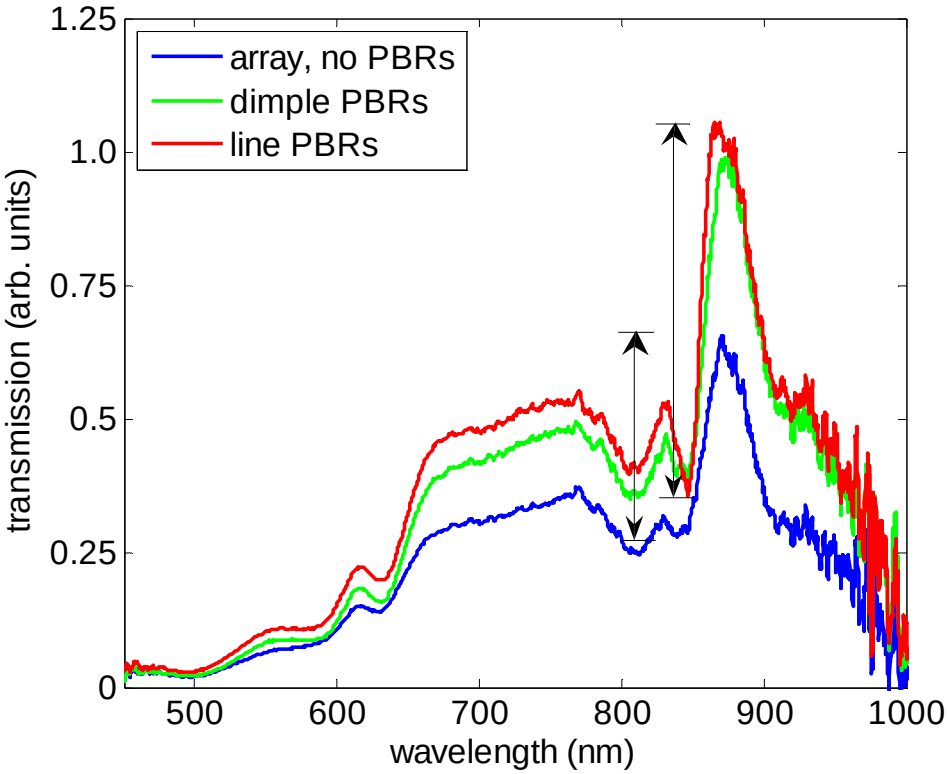

Figure 5.1: Transmission spectra of 800 nm arrays, with and without PBRs for horizontal polarization.

Figure 5.2 shows the transmission spectra of the array with and without PBRs for vertically polarized input. For vertical polarization, the array has a smaller (0,1) resonance because of the smaller extent of the array in this x direction. For this polarization the dimpled PBRs show negligible enhancement. While the line PBRs still

show significant enhancement, this enhancement is more pronounced for the (1,1) resonance than for the (0,1) resonance.

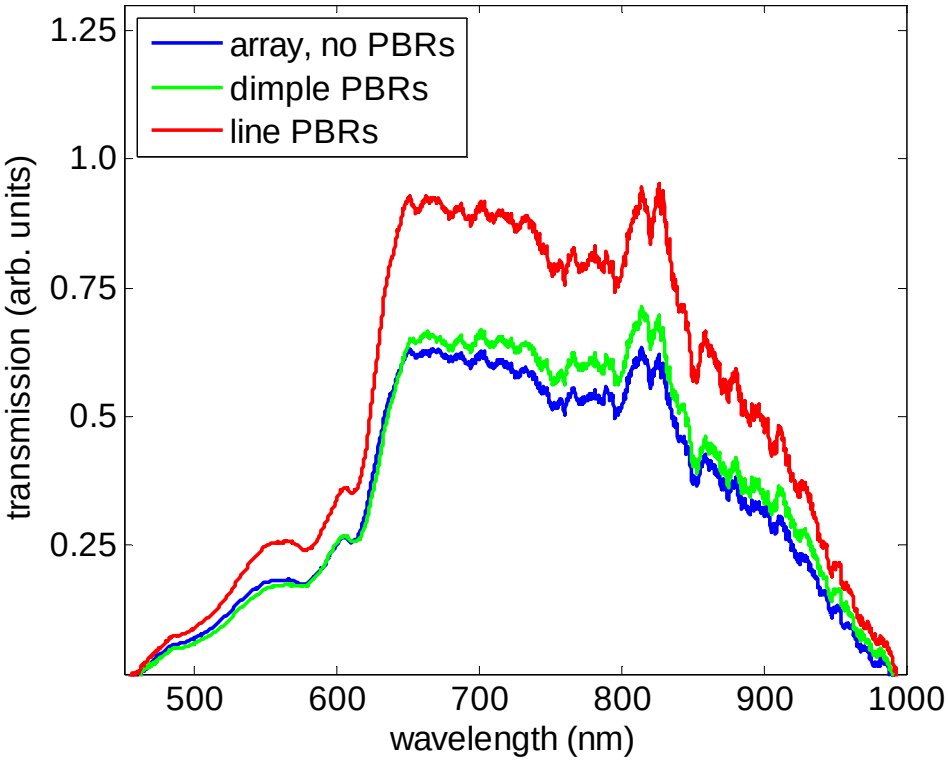

Figure 5.2: Transmission spectra of the 800 nm array with and without PBRs for vertically polarized light.

The SPPs generated at the edge of a nano-hole forms a dipole-like scattering pattern, where the SPP propagates in the direction of the electric field polarization for normally incident light [53, 54]. There is no light scattered perpendicular to the direction of the electric field polarization and that the maximum scattering occurs in the direction of the electric field polarization. A similar pattern is expected from the dimples. The lines scatter most efficiently for polarization perpendicular to its edge.

The enhanced (1,0) EOT for horizontal polarization comes form surface waves being generated at the nano-holes (leading to EOT) and then propagating in the direction of the electric field of the normally incident light. These surface waves are normally incident on the PBRs and they are reflected off the dimples or the lines. Subsequently, the reflected

surface waves are transmitted through the hole-array, in-phase with the EOT. The dimples give strong reflection because they have strong back-scattering of surface waves; therefore, the enhanced EOT is strong for both the arrays with the lined and the dimpled PBRs. For the (1,1) transmission and horizontal polarization, the dimples do not have as strong scattering at the 45 degree angle of this resonance, so their enhancement is reduced.

For the vertical polarization, the (0,1) EOT resonance sees no enhancement since the surface waves propagate in the vertical direction after the normally incident light is scattered from the holes, and so they do not impinge upon the PBRs. For the (1,1) resonance, there is a component of the surface waves at 45 degrees which propagates towards the PBRs and its reflected component is at -45 degrees. For the dimples, this reflected component is perpendicular to the incident wave, and so it does not exist in the dipole approximation. Therefore the dimples do not show enhanced EOT for the (1,1) resonance and y-polarization. For the lines, there is still a reflected component and so enhanced EOT is observed.

While the dimpled PBR has periodic-variation in the *y*-direction, the spacing is different from the *x*-direction. Therefore, if the dimpled PBR has a corresponding (1,1) resonance, it would be at a different wavelength to the (1,1) resonances of the hole-array. Therefore, this is not expected to enhance the EOT, and negligible enhancement was actually observed.

5.3 Variation of spacing between array and PBRs

Figure 5.3 shows the normalized peak transmission at 870 nm for different separations of the PBR layers from the hole array. The periodicity of the nano-hole array is 800 nm. Maximum transmission occurs when the PBRs are placed a half wavelength (400 nm) away. The minimum occurs close to when the reflectors are a wavelength away.

When the reflectors are placed a half wavelength away, the waves reflected by the PBRs and the surface waves propagating from the holes are in phase. Therefore, they interfere constructively and lead to maximum transmission.

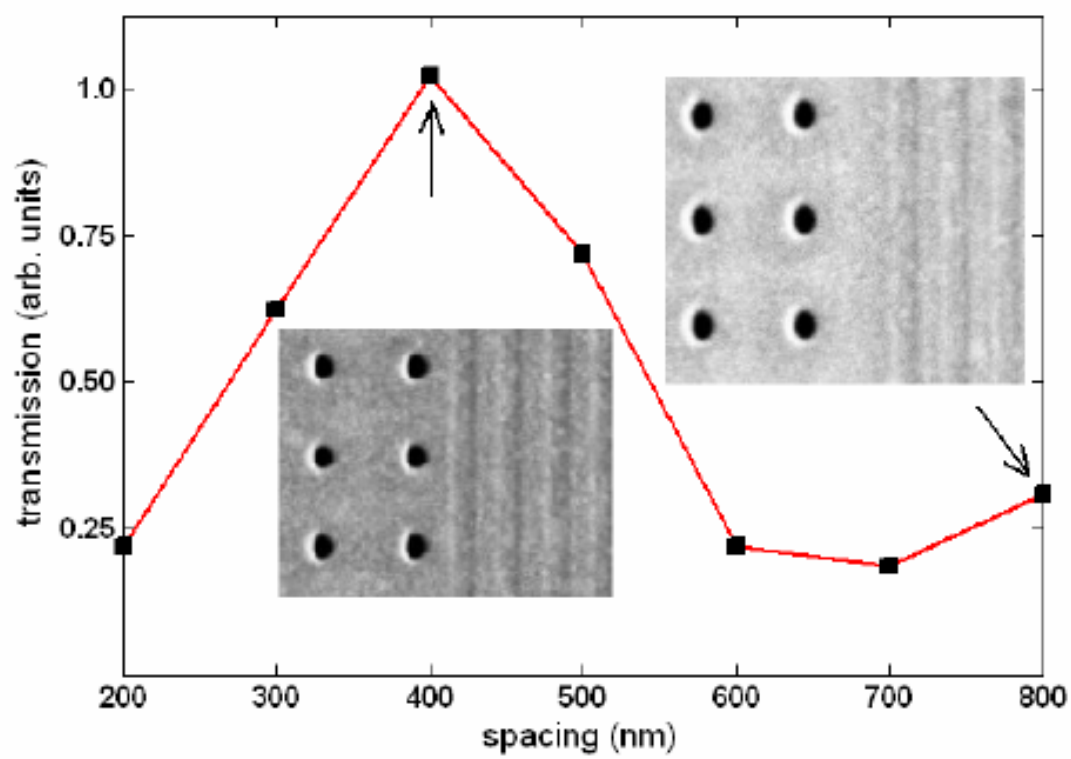

Figure 5.3: Transmission of nano-hole array at 867 nm with different separation of reflectors layers from array.

A roughly sinusoidal trend in the peak intensity is seen with spacing, with period equal to the array's periodicity. Thus, by judicious placement of the PBR layers, modulation of the transmission intensity can be achieved

5.4 Arrays flanked by PBRs on four sides

Figure 5.4 shows the transmission spectra of a 15 μm×15 μm array of holes with periodicity 800 nm, with and without PBRs. The resonance at 870 nm is enhanced by 1.5×, while the resonance at 800 nm is enhanced by nearly 2×. Again, the position of the resonances showed no significant change with the introduction of the PBRs. The PBRs in themselves did not exhibit any transmission.

Due to the symmetry of this structure, the polarization dependence exhibited by arrays with PBRs on two sides is not seen here.

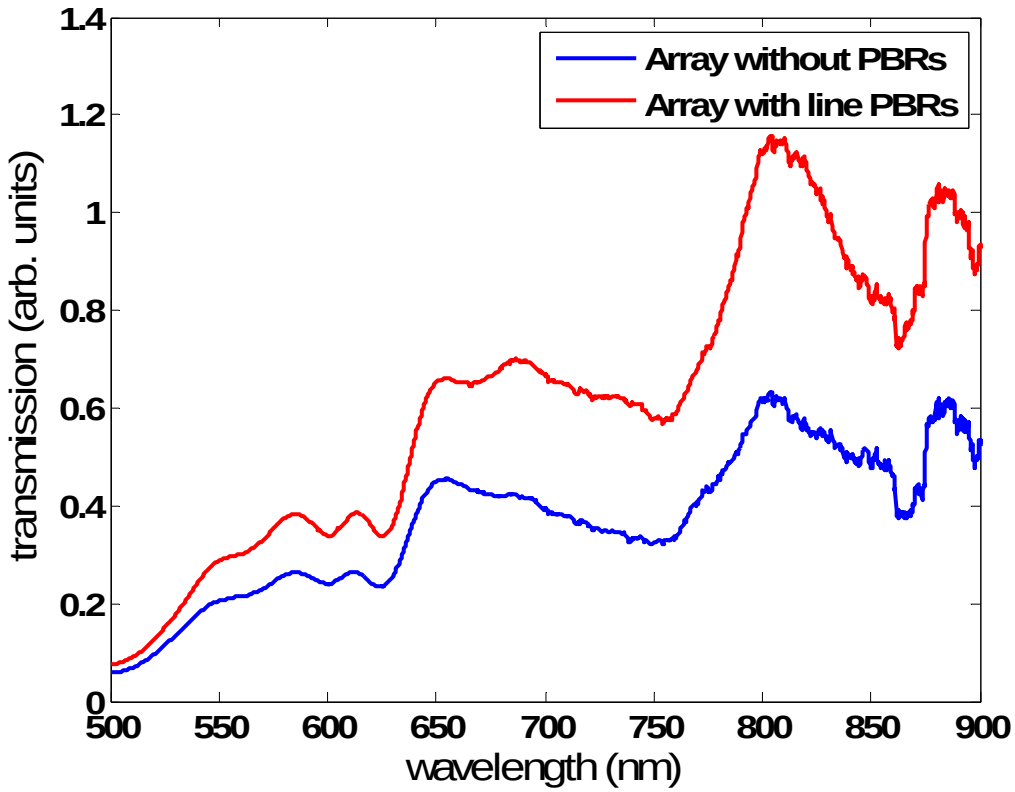

Figure 5.4: Transmission spectra of nano-hole array without and with reflectors on all four sides.

5.5 Isolation between nano-hole arrays

In order to determine the ability of the PBR structure to isolate adjacent arrays on a single substrate, two identical arrays were milled, separated by 1, 2, 3, 4 and 5 layers of line PBRs. Arrays without the PBRs, separated by un-patterned gold substrate were also fabricated. Figure 5.5 shows an SEM of the arrays separated by four layers of PBRs, and arrays with the same separation, without the PBRs. The arrays had holes of diameter 150 nm, and a periodicity of 700 nm. The arrays each covered an area of 7.5 μm×30 μm.

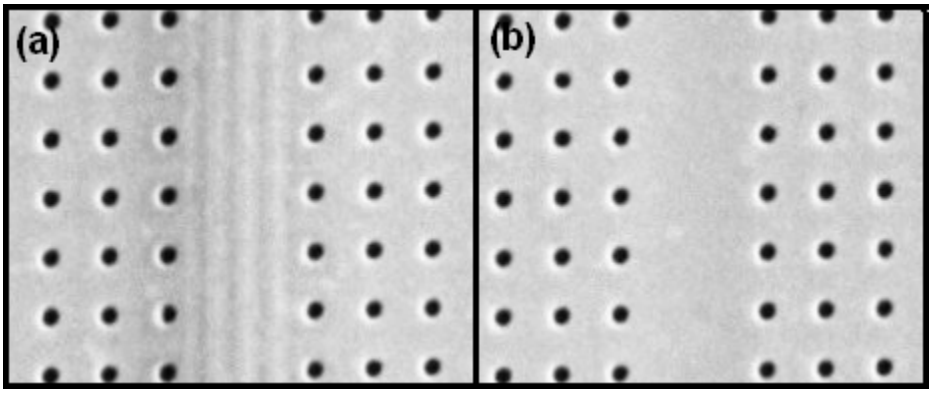

Figure 5.5: SEM of two arrays of periodicity 700 nm (a) separated by four PBR layers (b) separated by a spacing corresponding to four PBR layers, without PBRs.

The separation between the arrays is given by:

$$d = (n+1)\frac{\Lambda}{2} \qquad (5.1)$$

Where n is the number of PBR layers and Λ is the periodicity of the array.

For odd values of n, this separation corresponds to an integral multiple of the periodicity, and hence a constructive interference of SPs from each of the arrays. For an even number of reflector layers, this corresponds to a destructive interference between SPs from the arrays.

Figure 5.6 shows the white light transmission spectrum of two arrays separated by a spacing corresponding to five and four PBR layers, without and with PBRs. Figure 5.6(a) shows the constructive interference between two arrays separated by five layers of reflectors, and figure 5.6(b) shows the destructive interference between arrays separated by four PBR layers.

The effects of constructive and destructive interference is clear in the intensity of the (1,0) transmission resonance peak at 780 nm. The peak is higher when the arrays are separated by five PBR layers, than when the arrays are separated by four PBR layers. There is a 50% reduction in the peak intensity in the case with four PBR layers when compared to the case with five layers. With the introduction of PBRs, the case with four

PBR layers shows a 30% increase in the peak intensity, while the case with five PBRs shows a 10% reduction.

Since the PBRs are known to actually enhance transmission through arrays, the reduction in intensity in the case with constructive interference indicates that the PBR actually reduces the interference between the arrays. There are clearly two mechanisms at play in this study. First, there is an enhancement in the transmission of each of the arrays with the PBRs, as is evident in the four PBR sample. Secondly, the interference between the arrays is decreased in the five PBR case.

Since both arrays transmit, it is not easy to isolate the two mechanisms here. A straightforward inference as to whether the PBRs isolate adjacent arrays cannot be made with this experiment.

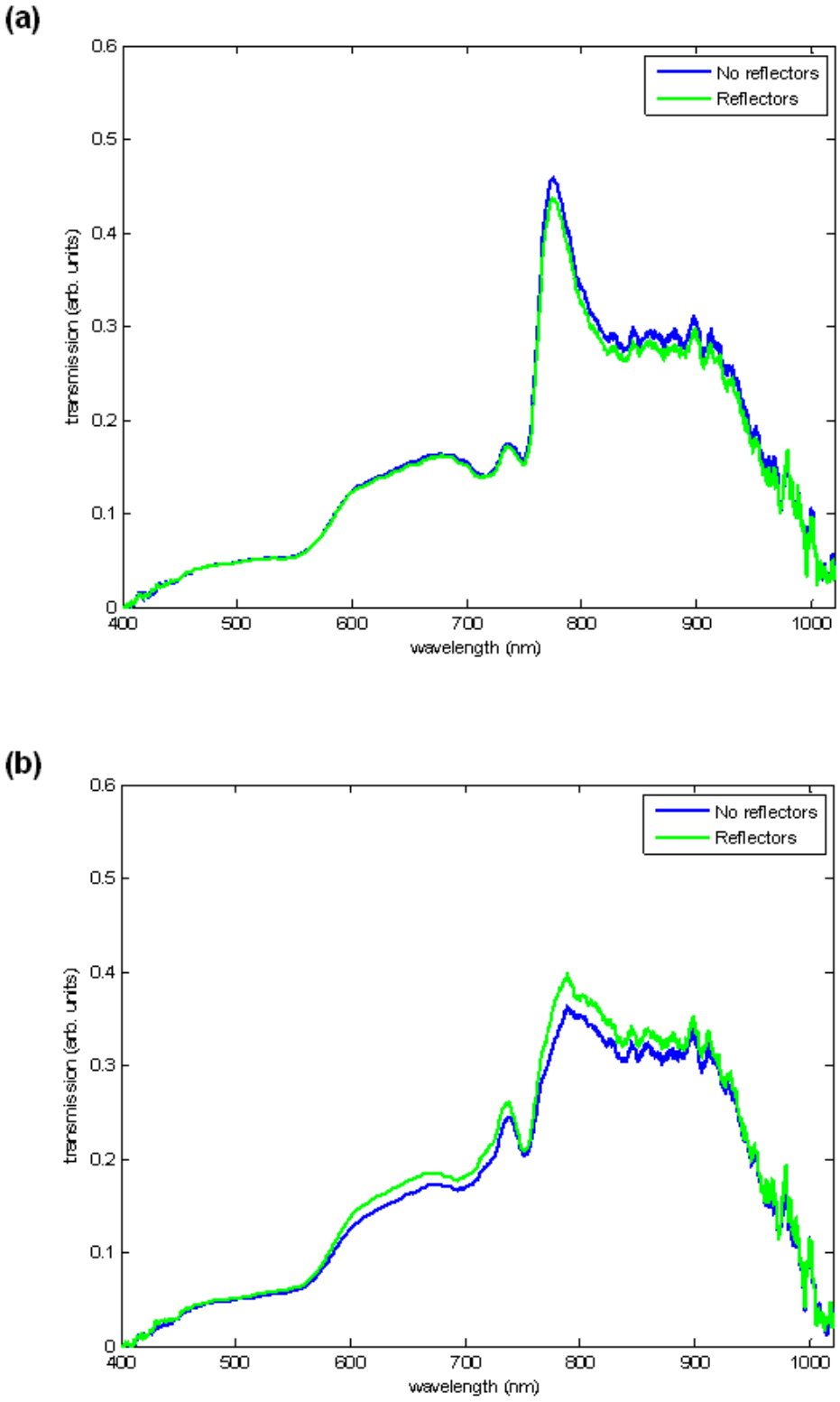

Figure 5.6: Transmission spectra of two arrays of nano-holes with periodicity 700 nm with separations corresponding to (a) five and (b) four PBR layers, with and without PBRs.

In order to better isolate the two effects, a structure is required to enable excitation of SPs without actually transmitting. The excited SPs can then propagate to an array fabricated in the vicinity. The intensity of transmission of propagated fields can then be studied to characterize the isolating capabilities of the PBRs. Figure 5.7 shows an SEM of an ensemble of a dimple array and hole array separated by PBR layers. SPs can be excited at the dimples by a coherent source. By properly polarizing the source, the SPs can be made to propagate towards the holes. This structure is currently being measured for isolation properties.

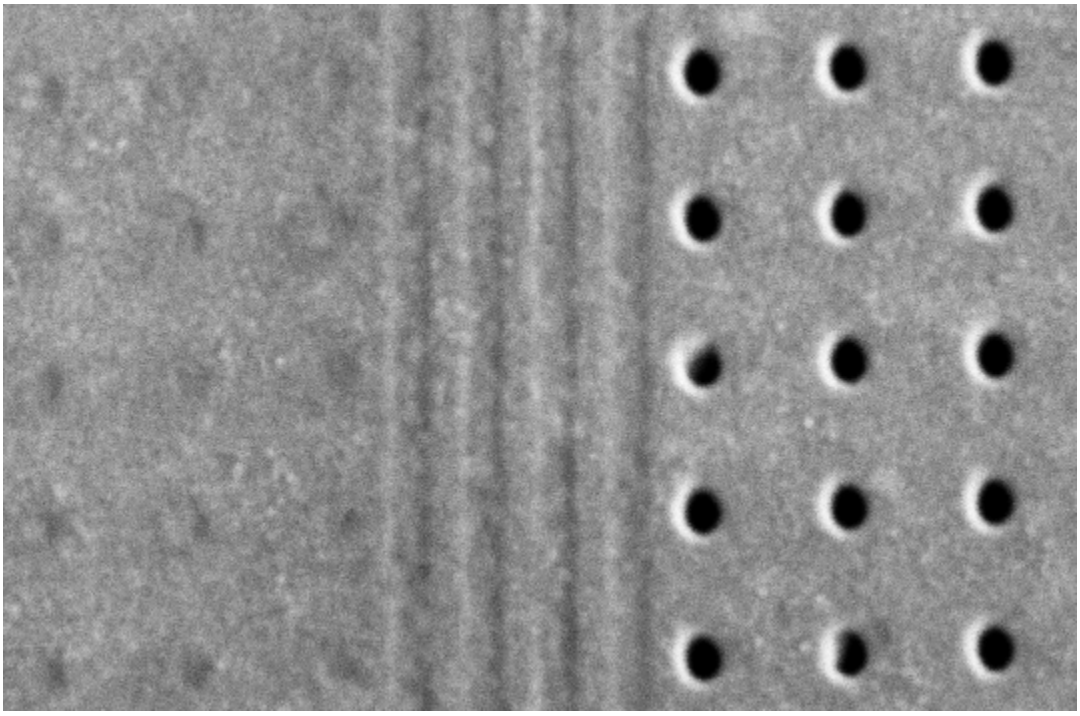

Figure 5.7: SEM of an ensemble of a dimple array and hole array of periodicity 700 nm separated by four PBR layers currently being studied for isolation properties.

5.6 Summary

Surface structures are presented to enhance EOT from nano-hole arrays. These structures have a periodicity equal to half the arrays periodicity, forming a Bragg reflector. They enhance EOT by recapturing scattered SPs and reflecting them back towards the array in phase with EOT light. The PBR structures show a high degree of

polarization dependence. Modulation of transmitted intensity is achieved by varying the separation between the array and PBRs. The polarization dependence of the PBR structure is eliminated by placing PBRs all around the nano-hole array. PBRs may be used for isolation of adjacent plasmonic devices.

5.7 Conclusion

In this chapter, the transmission spectra of nano-hole array with and without PBRs were presented. Enhancement in the transmission resonances due to the PBRs was seen. Modulation of the enhancement was seen with variation of the spacing between the array and the PBRs. Polarization sensitivity of the PBR structure was demonstrated. The polarization sensitivity can be overcome by placing PBRs all around the array, thus making the structure symmetric.

The PBRs enhance the EOT from a nano-hole array by reflecting the surface waves propagating away from the array in the direction of excitation, thus confining surface waves within the array. On a plasmonic integrated circuit, this can be used to effectively isolate adjacent structures by confining the surface waves from a structure within itself. This can help reduce unwanted coupling or cross talk between adjacent structures on a densely integrated chip.

Chapter 6

Quasicrystal nano-hole arrays

Introduction

In this chapter, experiments conducted on quasiperiodic nano-hole arrays are discussed. In section 5.1, the motivation behind the studies on the quasicrystal structure is presented. In section 5.2, the transmission resonances of the quasicrystal nano-hole array are discussed. In section 5.3, diffraction from the quasicrystal array is shown and polarization selectivity of the diffraction pattern is demonstrated. In section 5.4, results of FDTD calculations of a quasicrystal nano-hole array are presented.

6.1 Motivation

Quasicrystals provide interesting symmetries, even though they do not have a regular repeating pattern like other crystals. This makes quasicrystals useful for the manipulation of light, for example, for achieving rotationally invariant photonic band-gaps [49]. A ten-fold rotational symmetry has been observed in the diffraction pattern from a dielectric Penrose lattice [55]. Sharp resonances have been observed in the terahertz electromagnetic transmission through quasicrystal patterns of apertures in a metal [47]. Transmission resonances have also be observed in the optical regime in silver foils [46]. In the near-field, quasicrystal arrays have been used for subwavelength focusing [48].

These works did not study the diffraction properties of the quasicrystal. While rotational symmetries have been observed in diffraction patterns of quasicrystals, the properties of the diffraction from quasicrystals have not been studied. In this chapter, transmission spectra of quasiperiodic nano-hole arrays are presented, along with polarization control of diffraction from quasicrystals.

6.2 Transmission of quasicrystal nano-hole array

Figure 6.1 shows an SEM of the quasicrystal structure, and the transmission spectra of three quasicrystal nano-hole arrays. The side lengths of these Penrose rhombs were 700 nm, 800 nm and 900 nm. Transmission resonances for the 700 nm array were observed at 766 nm, 670 nm and 526 nm. The resonant wavelengths may be computed using the Fourier components of the stream file used to generate the structure and the relation

$$\lambda_r = \frac{2\pi}{G}\sqrt{\frac{\varepsilon_m(\lambda_r)\varepsilon_d}{\varepsilon_m(\lambda_r)+\varepsilon_d}} \qquad (6.1)$$

where λ_r are the resonant wavelengths obtained from wave-vector matching to the Fourier components, G , of the crystal structure and ε_d, $\varepsilon_m(\lambda_r)$ are the relative permittivity values of the dielectric on top of the gold, and the gold itself [4, 27]. When so computed, the resonant wavelengths fall at 720 nm, 620 nm and 500 nm. The resonances are clearly affected by the dispersion of the metal. Otherwise, the resonance at 526 nm would be expected at 383 nm if it were half the value of the longest wavelength as computed from the Fourier components.

In addition to the dispersion of the metal, due to the contribution of the quasiperiodic nature of the array, the prediction of the resonance positions is not straightforward. Other factors also contribute to the resonances such as resonance from within the holes [21] and evanescent waves at the surface of the metal [15].

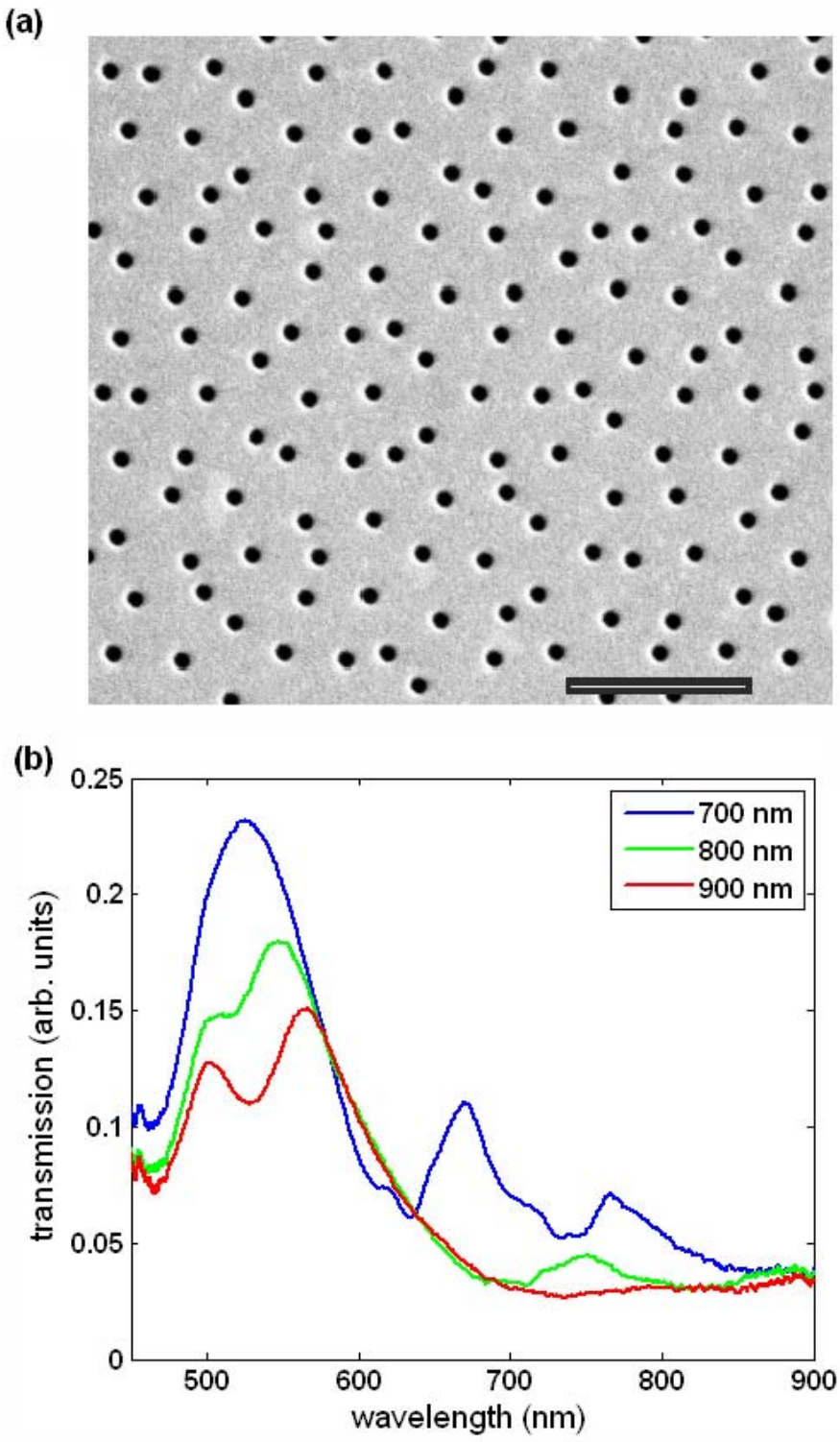

Figure 6.1: (a) SEM of the quasicrystal nano-hole array, scale bar corresponds to 2 μm. (b) Transmission spectra of quasicrystal nano-hole arrays of periodicity 700 nm, 800 nm and 900 nm.

Further understanding of the origin of the resonances may be obtained from the near field studies using FDTD calculations, as these have the capability of handling large structures [56].

6.3 Diffraction from quasiperiodic nano-hole array

Figure 6.2 shows the far field diffraction pattern of the quasicrystal nano-hole array, and the Fourier transform of the stream file used to fabricate the structure. A ten-fold rotational symmetry is observed in the pattern, which conforms to the Fourier transform. A 36 degree angle is seen between diffraction lobes, which matches the data corresponding to the Fourier transform, and the diffraction patterns previously seen for Penrose lattice structures with five fold rotational symmetry [55]. The three distinct rings of the diffraction patterns have lobes making angles of 31 degrees, 39 degrees and 51 degrees with respect to zeroth order transmission direction.

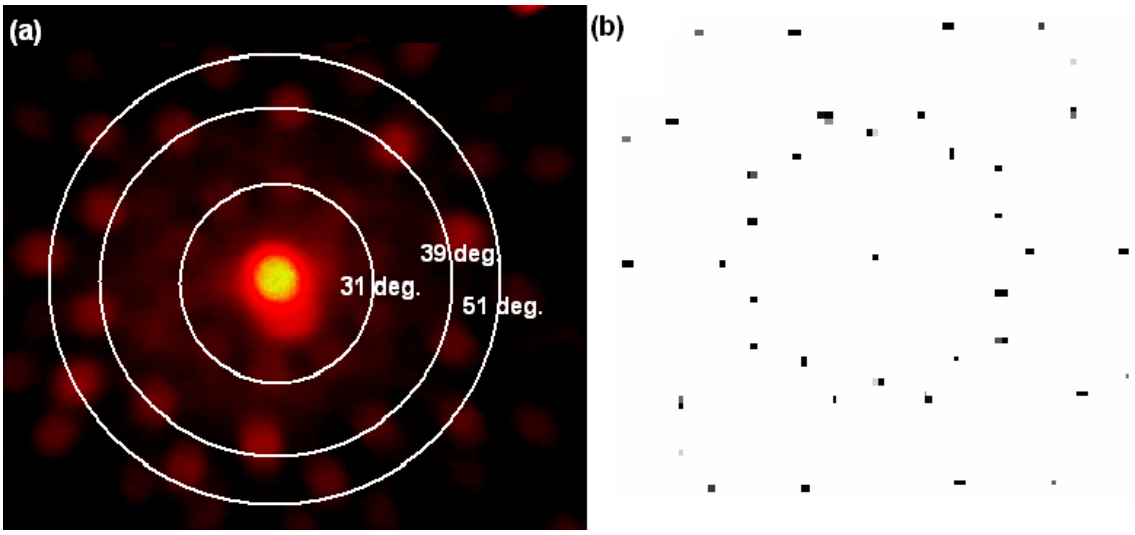

Figure 6.2: (a) He-Ne diffraction pattern from a quasicrystal nano-hole array, with angles made by the rings of lobes marked. (b) Fourier transform of corresponding stream file.

The diffraction pattern obtained was small. Therefore, to better resolve the observed pattern, a small angle of incidence was used. By doing this, only a portion of the

diffraction pattern was observed. The lobes seen in this partial pattern oriented themselves along the direction of polarization of the incident beam. When the polarization was rotated, the most intense lobes of the diffraction pattern rotated along with the axis of polarization to re-orient themselves along the new direction of polarization.

This polarization dependence of the diffraction pattern becomes more apparent with a larger angle of incidence. Figure 6.3 shows the diffraction pattern observed form the 700 nm quasicrystal array for two angles of non-normal incidence. Figures 6.3 (a) and (b) show the diffraction patterns for a very small angle of incidence, for orthogonal polarizations. Figures 6.3 (c) and (d) show the pattern for a larger angle of incidence for orthogonal polarizations. As seen in Figure 6.3 (c) and (d), a smaller portion of the entire diffraction pattern is observed with a larger incidence angle. The lobes seen in the partial pattern under this condition are only those that lie along the direction of polarization.

The polarization-dependent control of the diffraction pattern can be explained in terms of the excitation of surface waves or SPs with different polarizations. It has been demonstrated that SPPs scattered from nanoholes have directional symmetry that is aligned with the polarization of the incident beam [53, 57]. The surface waves aligned with the input polarization are responsible for the diffraction pattern observed; thereby the polarization determines which lobes of the quasicrystal diffraction pattern are excited. This phenomenon is particularly interesting for quasicrystals because of their high-order rotational symmetry – the diffraction pattern orientation corresponds directly to the polarization of the incident beam. A similar rotation of the diffraction pattern was not observed for a square array of nano-holes and has not been reported for electron diffraction patterns of quasicrystals [58].

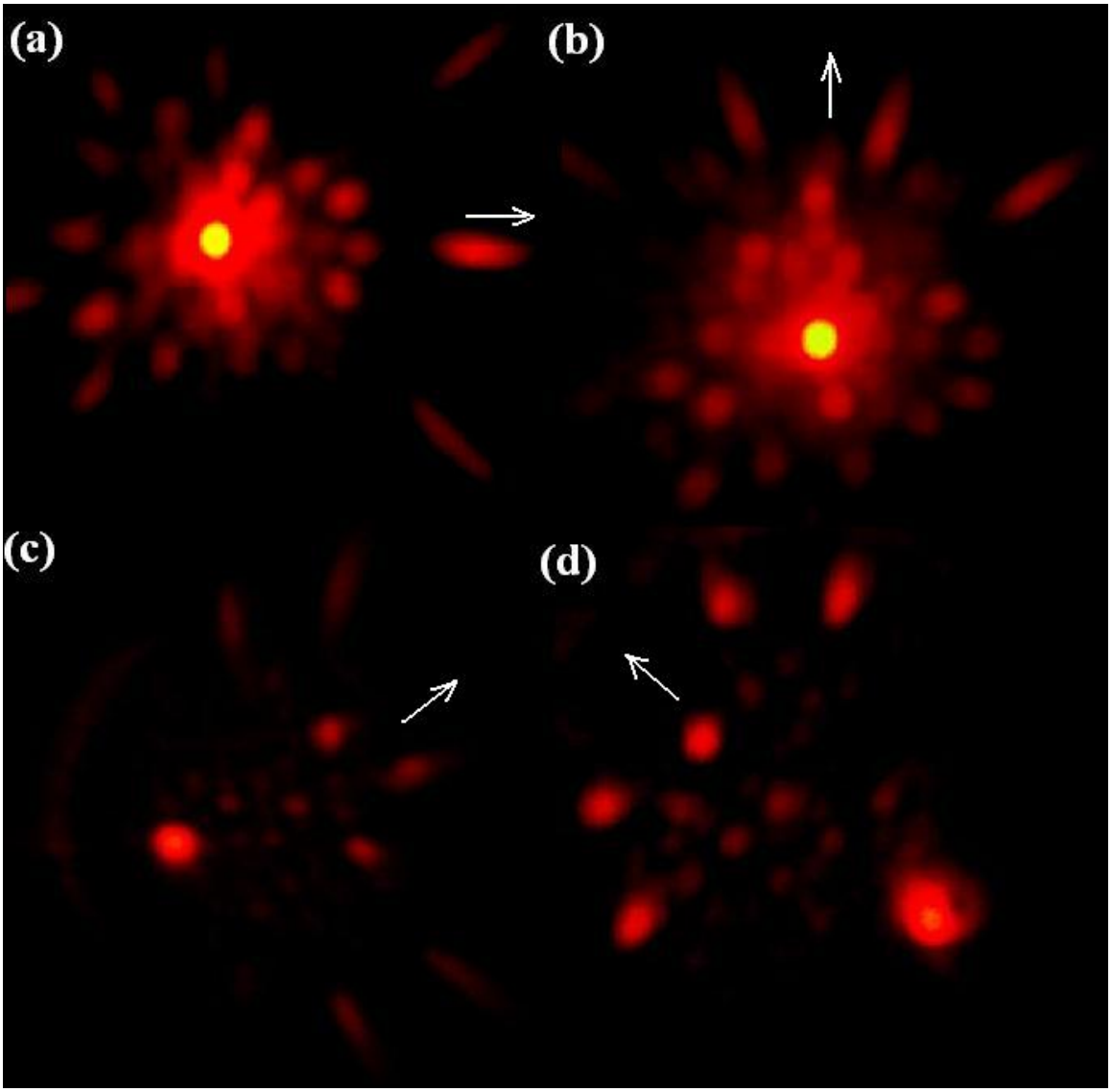

Figure 6.3: Partial diffraction patterns from the 700 nm quasicrystal nano-hole array for (a) and (b) small angle of incidence (c) larger angle of incidence. The direction of polarization in each case is indicated by arrows.

The polarization control of diffraction from a quasicrystal is unique, as such control of diffraction patterns has not been reported so far for optical diffraction in two dimensional dielectric quasicrystals [55] or in electron diffraction of quasicrystal [58].

6.4 FDTD analysis of quasicrystal nano-hole arrays

FDTD analysis of quasicrystals is a useful method to obtain better insight into the physical mechanisms behind the observed characteristics, because FDTD analyses have been proven capable of handling intense electromagnetic problems such as arbitrary structures [56].

FDTD simulations of the 700 nm quasicrystal array were set up with 20 nm grids in the X and Y directions and a 3 nm grid in the Z direction, which is normal to the gold surface. The 3 nm grid was chosen to better capture the exponentially decaying SP fields [24]

Figure 6.4 shows the transmission spectrum of the 700 nm array as computed using FDTD calculations. The experiment showed transmission resonances at 526 nm, 670 nm and 766 nm. The computed resonances fall at 550 nm, 650 nm and 750 Nm. There is a fourth resonance at 850 nm which is not seen in the experimental spectrum. It can be explained that the fourth resonance is lost in the experimental noise threshold. The positions of the other three resonances agree quite well with the computed resonance wavelengths.

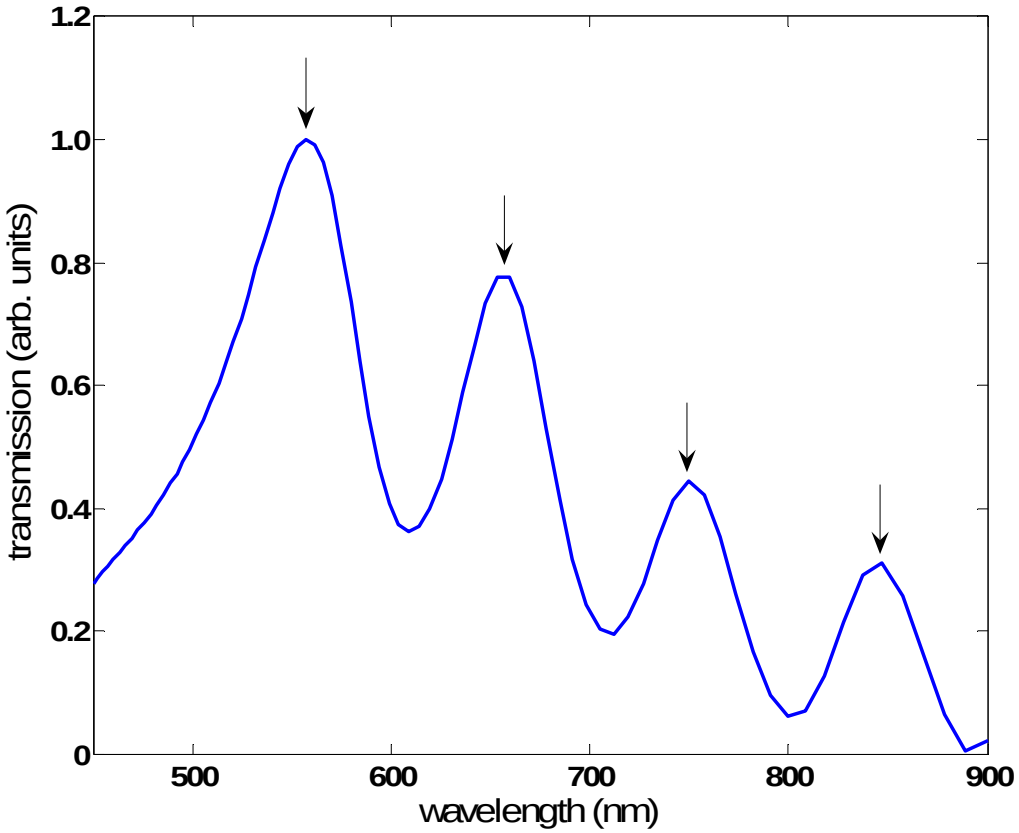

Figure 6.4: FDTD computed transmission spectrum of the 700 nm array. Four resonances are seen at 550 nm, 650 nm, 750 nm and 850 nm.

Figure 6.5 shows the far field pattern computed at 632 nm for horizontally polarized input. The higher intensity of the lobes aligned with the input polarization is clearly seen from the diffraction pattern. A similar alignment of intense lobes was seen for the far field computed for vertically polarized light.

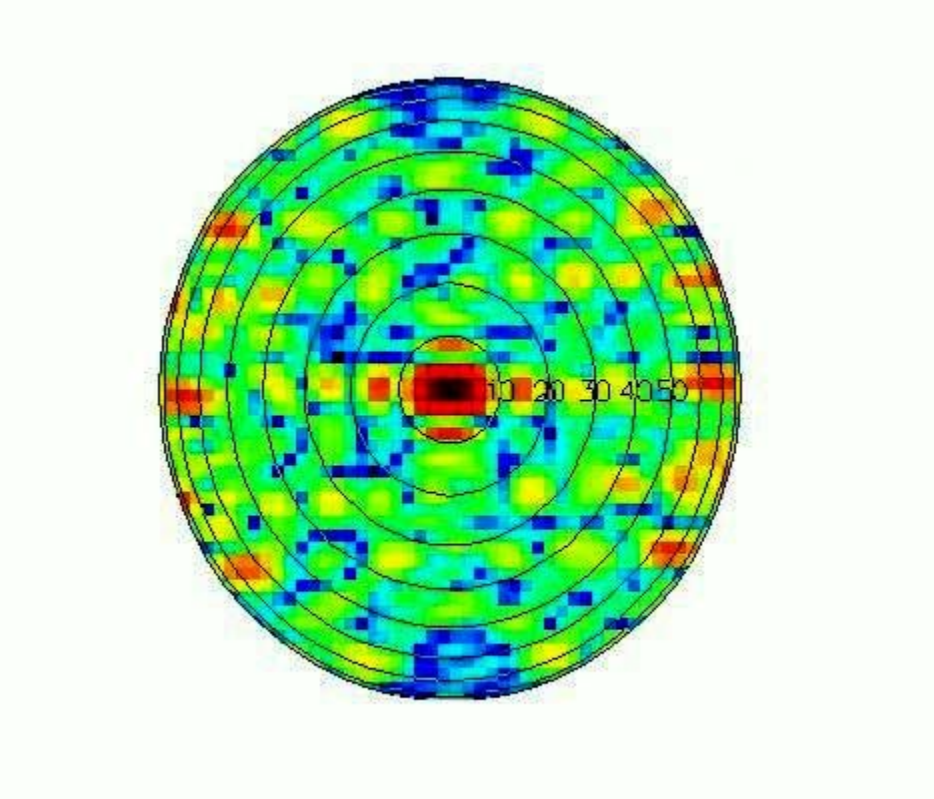

Figure 6.5: FDTD computed far field diffraction pattern at 632 nm for horizontally polarized input. Lobes aligned with the direction of polarization are seen to be more intense than others.

Figure 6.6 shows plots of field intensity versus position at the 650 nm resonance wavelength. The excitation was horizontally polarized, or polarized along the x direction. The field intensity of the three components of the surface wave namely, E_x, H_y and E_z fields are plotted. It can be seen that some holes display higher field intensities than other holes. This leads to hot-spots in the structure where intense focusing of fields occurs. This can be used for applications like SERS. Hot-spots are also observed for the anti-resonances, which does not occur for periodic structures. For isolated holes, FDTD caulculations will show high field intensity corresponding to the LSPR, and not for other wavelengths.

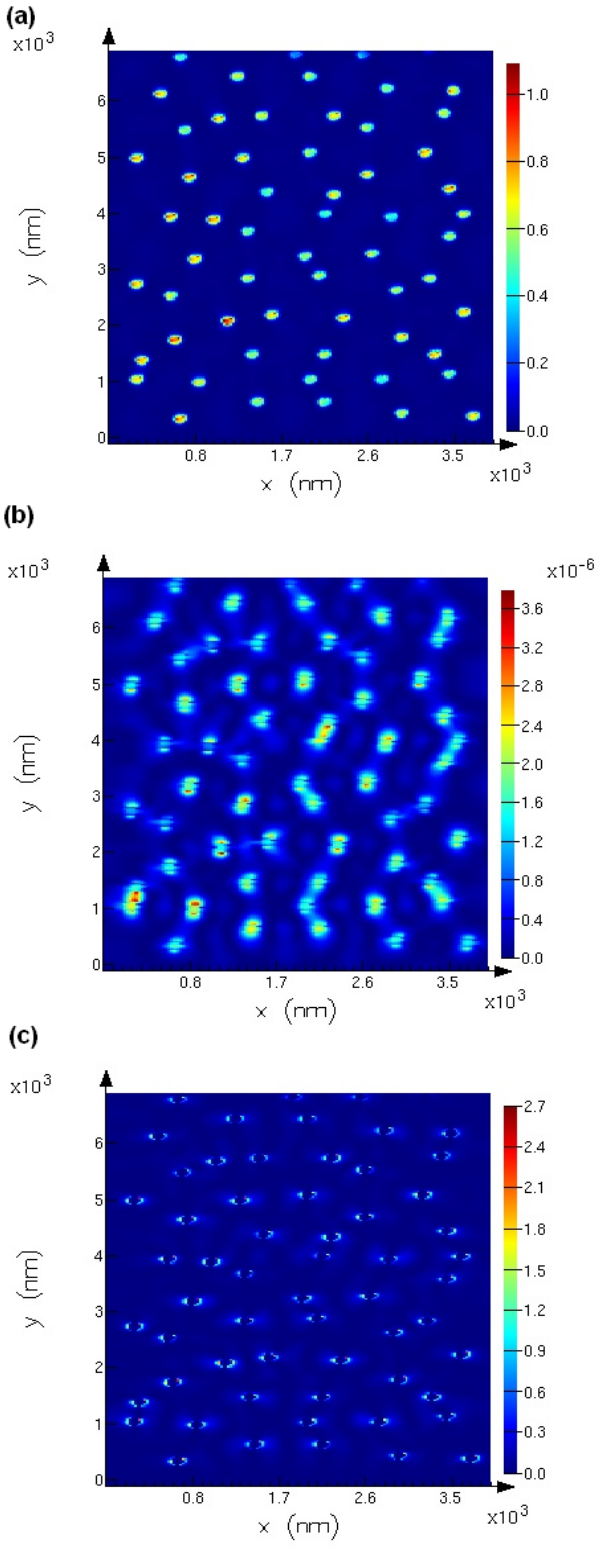

Figure 6.6: Field intensity Vs position for the quasicrystal structure, at the 650 nm resonance. The fields are plotted for horizontal or x-polarized input (a) E_x field intensity, (b) H_y field intensity and (c) E_z field intensity.

6.5 Summary

Resonances in the transmission through quasiperiodic nano-hole arrays were seen. The resonant wavelengths are strongly influenced by the dispersion of the metal in the optical regime, and are not predicted by simple SP wave vector matching. Anticipated ten-fold rotational symmetry is seen in the diffraction pattern, with angles of 36 degrees between adjacent lobes.

A unique polarization dependence is seen in the partial diffraction pattern obtained for non-normal incidence. The lobes of the partial pattern follow the polarization of the excitation beam.

FDTD calculations of the quasicrystal structure were performed. Computed transmission resonances show good agreement with experiment. The polarization dependence is seen in the computed far field pattern. Near field plots show formation of hot spots at the resonant and non-resonant wavelengths, with certain holes in the array showing more intense fields than others.

6.6 Conclusions

In this chapter, experimental and theoretical results on the quasicrystal nano-hole structure were presented. Resonant transmission was observed. Polarization control of the diffraction pattern was seen. Good agreements were obtained between the theoretical model and experiment.

Chapter 7

Conclusions

The PBR structure has been shown to enhance EOT by reflecting the SPs scattering away from the array. This structure confines SPs to the extent of the array. It is capable of minimising loss in the form of scattered SPs. The PBR structure was seen to exhibit polarization sensitivity. Modulation of transmission was achieved by varying the separation between the array and PBRs.

The results presented in chapter 5 have been published.

- P. Marthandam and R. Gordon (2007), "Plasmonic Bragg reflectors for enhanced extraordinary optical transmission through nano-hole arrays in a gold film", Optics Express, Vol. 15 Issue 20, pp. 12995-13002.
- P. Marthandam and R. Gordon (2007),"Plasmonic Bragg reflectors for sub-wavelength hole arrays in a metal film", Proceedings of the 20th Annual meeting of IEEE LEOS, October 2007, Lake Buena Vista, FL.

In order to further study the PBR structures, the effect of reflectors' depth, and number of reflector layers could be analysed. An efficient way to measure the PBR layers' ability to isolate arrays needs to be developed.

The PBRs can be made to increase local field intensities of isolated apertures. They could thus be used in sensing applications.

The unique ability to control diffraction from the quasicrystal nano-hole array by changing input polarization was demonstrated. The formation of hot-spots within the array, with some holes having higher field intensities than others was observed.

The experimental results presented in chapter 6 have been presented as a paper and accepted for publication:

- P. Marthandam and R. Gordon, “Polarization controlled diffraction from a quasicrystal nano-hole array in a gold film”. Accepted for publication in Journal of Optics A.

The polarization sensitive properties can be used in the detection of polarization state of a system. For a structure with five-fold symmetry, the lobes of the diffraction pattern are separated by 36 degrees. By fabricating structures with higher orders of rotational symmetry, this step can be reduced greatly, and the system used as a polarization detector.

The hot-spots formed under resonance conditions can be put to use in spectroscopic applications like SERS, and in sensors.

Bibliography

1. Maier, S.A., *Plasmonics: The promise of highly integrated optical devices.* IEEE Journal of Special Topics in Quantum Electronics, 2006. **12**(6): p. 1671-1677.
2. Ozbay, E., *Plasmonics: Merging photonics and electronics at nanoscale dimensions.* Science, 2006. **311**: p. 189-193.
3. http://www.diss.fu-berlin.de/2003/73/chapter_3.pdf.
4. Raether, H., *Surface plasmons*. 1988, Berlin: Springer-Verlag.
5. Solymar, L. and Walsh, D., *Lectures on the electrical properties of materials*. 1984: Oxford University Press.
6. Ebbesen, T.W., Lezec, H. J., Ghaemi, H. F., Thio, T. and Wolff, P. A., *Extraordinary optical transmission through sub-wavelength hole arrays.* Nature, 1998. **391**(12): p. 667-669.
7. Bethe, H., *Theory of diffraction by small holes.* The Physical Review, 1944. **66**(7): p. 163-182.
8. Grupp, D.E., Lezec, H. J., Thio, T. and Ebbesen, T. W., *Beyond the Bethe limit:Tunable enhanced light transmission through a single sub-wavelength aperture.* Advanced Materials, 1999. **11**(10): p. 860-862.
9. DiMaio, J.R. and Ballato, J., *Polarization dependent transmission through subwavelength anisotropic aperture arrays.* Optics Express, 2006. **14**(6): p. 2380-2384.
10. Airola, M. and Blair, S., *Second harmonic generation from an array of sub-wavelength metal apertures.* Journal of Optics A, 2005. **7**: p. 118-123.
11. Baida, F.I., van Labeke, D. and Guizal, B., *Enhanced confined light transmission by single subwavelength apertures in metallic films.* Applied Optics, 2003. **42**(34): p. 6811-6815.
12. Moskovits, M., *Surface enhanced spectroscopy.* Reviews of Modern Physics, 1985. **57**(3): p. 783-828.
13. Ghaemi, H.F., Thio, T., Grupp, D. E., Ebbesen, T. W. and Lezec, H. J., , *Surface plasmons enhance optical transmission through subwavelength holes.* Physical Review B, 1998. **58**(11): p. 6779-6782.
14. Treacy, M.M.J., *Dynamical diffraction explanation of the anamolous transmission of light through metal gratings.* Physical Review B, 2002. **66**.
15. Lezec, H.J. and Thio, T., *Diffracted evanescent wave model for enhanced and suppressed optical transmission through subwavelength hole arrays.* Optics Express, 2004. **12**(16): p. 3629-3651.
16. Cao, Q. and Lalanne, P., *Negative role of surface plasmons in the transmission of metallic gratings with very narrow slits.* Physical Review Letters, 2002. **88**(5).

17. Gordon, R., Brolo, A. G., McKinnon, A., Rajora, A., Leathem, B. and Kavanagh, K. L., *Strong polarization in the optical transmission through elliptical nano-hole arrays.* Physical Review Letters, 2004. **92**(3).
18. Gordon, R., Hughes, M., Leathem, B., Kavanagh, K. L. and Brolo, A. G., *Basis and lattice polarization mechanisms for light transmission through nano-hole arrays in a metal film.* Nano Letters, 2005. **5**(7): p. 1243-1246.
19. Koerkamp, K.J.K., Enoch, S., Segerink, F. B., van Hulst, N. F. and Kuipers, K. L., *Strong influence of hole shape on extraordinary transmission through periodic arrays of subwavelength holes.* Physical Review Letters, 2004. **92**(18).
20. van der Molen, K.L., Koerkamp, K. J. K, Enoch, S., Segerink, F. B., van Hulst, N. F. and Kuipers, K. L., *Role of shape and localized resonances in extraordinary transmission through periodic arrays of subwavelength holes: Experiment and theory.* Physical Review B, 2005. **72**: p. 045421.
21. Degiron, A., Lezec, H. J., Yamamoto, N. and Ebbesen, T. W., *Optical transmission properties of a single subwavelength aperture in a real metal.* Optics Communications, 2004. **239**: p. 61-66.
22. Homola, J., Yee, S. S. and Gauglitz, G., *Surface plasmon resonance sensors: review.* Sensors and Actuators B, 1999. **54**: p. 3-15.
23. Gordon, R. and Brolo, A. G., *Increased cut-off wavelength for a subwavelength hole in a real metal.* Optics Express, 2005. **13**(6): p. 1933-1938.
24. Gordon, R., Kumar, L. K. S. and Brolo, A. G., *Resonant light transmission through a nano-hole in a metal film.* IEEE Transactions on Nanotechnology, 2006. **5**(3): p. 291-294.
25. Croswell, W.F., Rudduck, R. C. and Hatcher, D. M., *The admittance of a rectangular waveguide radiating into a dielectric slab.* IEEE Transactions on Antennas and Propagation, 1967. **15**(5): p. 627-633.
26. MacPhie, R.H. and Zaghloul, A. I., *Radiation from a rectangular waveguide with infinite flange- Exact solution by the correlation matrix method.* IEEE Transactions on Antennas and Propagation, 1980. **28**(4): p. 497-503.
27. Johnson, P.B. and Christy, R. W., *Optical constants of noble metals.* Physical Review B, 1972. **6**(12): p. 4370-4379.
28. Kumar, L.K.S., Lesuffleur, A. and Gordon, R., *Double nanohole apex-enhanced transmission in metal films.* Applied Physics B, 2006. **84**: p. 25-28.
29. Lesuffleur, A., Kumar, L. K. S. and Gordon, R., *Enhanced second harmonic generation from nanoscale double-hole arrays in a gold film* Applied Physics Letters, 2006. **88**.
30. Schuck, P.J., Fromm, D. P., Sundaramurthy, A., Kino, G. S. and Moerner, W. E., *Improving the mismatch between light and nano-scale objects with gold bowtie antennas.* Physical Review Letters, 2005. **94**.
31. Stockman, M.I., *Nanofocusing of optical energy in tapered plasmonic waveguides.* Physical Review Letters, 2004. **93**: p. 137404.
32. Chen, C.K., de Catsro, A. R. B. and Shen Y. R., *Surface enhanced second harmonic generation.* Physical Review Letters, 1981. **46**(2): p. 145-148.
33. Kneipp, K., Kneipp, H., Itzkan, I., Dasari, R. R. and Feld, M. S., *Ultrasensitive chemical analysis by Raman spectroscopy.* Chemical Reviews, 1999. **99**(10): p. 2957-2976.

34. Brolo, A.G., Arctander, E., Gordon, R., Leathem, B. and Kavanagh, K. L., *Nano-hole enhanced Raman scattering.* Nano Letters, 2004. **4**(10): p. 2015-2018.
35. Brolo, A.G., Kwok, S. C., Moffitt, M. G., Gordon, R., Riordon, J. and Kavanagh, K. L., *Enhanced fluorescence from arrays of nano-holes in a gold film.* Journal of the American Chemical Society, 2005. **127**: p. 14936-14941.
36. Nice, E.C. and Catimel, B., *Instrumental biosensors: New perspectives for the analysis of biomolecular interactions.* BioEssays, 1999. **21**(4): p. 339-352.
37. Brolo, A.G., Gordon, R., Leathem, B. and Kavanagh, K. L., *Surface plasmon resonance sensor based on the enhanced light transmission through arrays of nano-holes in gold films.* Langmuir, 2004. **20**: p. 4813-4815.
38. Dittrich, P.S., Tachikawa, K. and Manz, A., *Micro total analysis systems: Latest advancements and trends.* Analytical Chemistry, 2006. **78**: p. 3887-3908.
39. De Leebeeck, A., Kumar, L. K. S., de Lange, V., Sinton, D., Gordon, R. and Brolo, A. G., *On-chip surface-based detection with nanohole arrays.* Analytical Chemistry, 2007. **79**: p. 4094-4100.
40. Lesuffleur, A., Im, H., Lindquist, N. C. and Oh, S-H., *Periodic nano-hole arrays with shape enhanced plasmon resonance as real time biosensors.* Applied Physics Letters, 2007. **90**.
41. Garcı´a-Vidal, F.J., Lezec, H. J., Ebbesen, T. W. and Martı´n-Moreno, L., *Multiple paths to enhance optical transmission through a single subwavelength slit.* Physical Review Letters, 2003. **90**.
42. Martı´n-Moreno, L., Garcı´a-Vidal, F. J., Lezec, H. J., Degiron, A. and Ebbesen, T. W., *Theory of highly directional emission from a single subwavelength aperture surrounded by surface corrugations.* Physical Review Letters, 2003. **90**.
43. Thio, T., Pellerin, K. M., Linke, R. A., Lezec, H. J. and Ebbesen, T. W., *Enhanced light transmission through a single subwavelength aperture.* Optics Letters, 2001. **26**(24): p. 1972-1974.
44. Lezec, H.J., Degiron, A., Devaux, E., Linke, R. A., Martı´n-Moreno, L., Garcı´a-Vidal, F. J. and Ebbesen, T. W., *Beaming light from a subwavelength aperture.* Science, 2002. **297**: p. 820-822.
45. Kim, D.S., Hohng, S. C., Malyarchuk, V., Yoon, Y. C., Ahn, Y. H., Yee, K. J., Park, J. W., Kim, J., Park, Q. H. and Lienau, C., *Micropscopic origin of surface plasmon radiation in plasmonic band gap nanostructures.* Physical Review Letters, 2003. **91**.
46. Przybilla, F., Genet, C. and Ebbesen, T. W., *Enhanced transmission through Penrose subwavelength hole arrays.* Applied Physics Letters, 2006. **89**: p. 121115.
47. Matsui, T., Agrawal, A., Nahata, A. and Valy Vardeny, Z., *Transmission resonances through aperiodic arrays of subwavelength apertures.* Nature, 2007. **446**: p. 517-521.
48. Huang, F.M., Zheludev, N., Chen, Y. and de Abajo, F. J. G., *Focusing of light by a nanohole array.* Applied Physics Letters, 2007. **90**.
49. Chan, Y.S., Chan, C. T. and Liu, Z. Y., *Photonic bandgaps in two dimensional photnonic quasicrystals.* Physical Review Letters, 1998. **80**: p. 956-959.
50. Penrose, R., *Set of tiles covering a surface*, U.P. Office, Editor. 1976: United States.

51. Schweber, I., http://www.math.ubc.ca/~cass/courses/m308-02b/projects/schweber/penrose.html.
52. de Bruijn, N.G., *Updown generation of Penrose patterns.* Indagationes Mathematicae, 1990. **1**(2): p. 201-220.
53. Sönnichsen, C., Durch, A. C., Steininger, G., Koch, M., von Plassen, G. and Feldmann, J., *Launching surface plasmons into nanoholes in metal films.* Applied Physics Letters, 2000. **76**(2): p. 140-142.
54. Brun, M., Drezet, A., Mariette, H., Chevalier, N., Woehl, J. C. and Huant, S., *Remote optical addressing of single nano-objects.* Europhysics Letters, 2003. **64**: p. 634-640.
55. Krauss, F. and De La Rue, R. M., *Photonic crystals in the optical regime- Past, present and future.* Progress in Quantum Electronics, 1999. **23**(2): p. 51-96.
56. Hughes, M.C. and Gordon, R., *Optical transmission properties and enhanced loss for randomly positioned apertures in a metal film.* Applied Physics B, 2007. **87**(2): p. 239-242.
57. Yin, L., Vlasko-Vlasov, V. K., Rydh, A., Pearson, J, Welp, U., Chang, S. H., Gray, S. K., Schatz, G. C., Brown, D. B., Kimball, C. W., *Surface plasmons at single nanoholes in Au films.* Applied Physics Letters, 2004. **85**(3): p. 467-469.
58. Diehl, R.D., Lidieu, J., Ferralis, N., Szmodis, A. W. and McGrath, R., *Low-energy electron diffraction from quasicrystal surfaces.* Journal of Physics: Condensed Matter, 2003. **15**(3): p. 63-81.

Appendix A

Stream files

A stream file fed into the CAD interface of the FIB will have an extension of .str. A typical stream file will start like this:

s
6
384120
50 17 23
50 17 25
50 17 27
50 17 29
50 17 31
50 17 79
50 17 81
50 17 83
50 17 85
50 17 87
50 17 135
50 17 137
50 17 139

The first character indicates that what follows is a stream file.

The number that follows is referred to as loop count. This indicates how many times the FIB will have to loop the stream file. In this case, it means that the machine will mill each pixel specified in this stream file six times.

The number that follows this is the total number of pixels to be milled. This is limited to one million.

Each line following this has three numbers. The first number is the beam dwell time in ns. The two other numbers specify the x and y coordinates of the pixel to be milled.

Appendix B

Script file for array with line PBR on two sides

```
%%%%%%%%%%%%%%%%%%%%%%%%%%%%%%%%%%%%%%%%
% Filename: PBRScript.m
% Author: Pramodha Marthandam
% Date created: 12 June 2007
% Structure details: Array of circular holes, about 15umX30nm, flanked
% by gratings, with half the periodicity of the hole array
%%%%%%%%%%%%%%%%%%%%%%%%%%%%%%%%%%%%%%%%

%Defining the nanometer to pixel conversion factor
NPixCon=7.14;

% Pixel Matrix
PixMat = zeros(4096,4096,'uint16');

% Opening the file input.txt and reading dimensional parameters
num = textread('input.txt','%u%*[^\n]');

% Extracting the parameters from the input file

% Hole diameter
Dia=num(1);

% Resonance wavelength (periodicity)
Per=num(2);

% Dwell times of hole and grating
BTime1=num(3);
```

```
BTime2=num(4);

% Pixel skip factor
PSkip=num(5);

% Conversion from nanometers to pixels
DiaPix=uint16(Dia/NPixCon);
RadPix=DiaPix/2;
PerPix=uint16(Per/NPixCon);

Rad=uint16(Dia/2);
ArrayMid=4096/2;

XX=0;
for y=(10+RadPix):PerPix:4096
   for x=(ArrayMid/2 +RadPix):PerPix:(ArrayMid+(ArrayMid/2))
      PixMat(x,y)=BTime1;
      if (x>XX)
         XX=x;
      end
      for yPix=y:PSkip:(y+RadPix)
         for xPix=x:PSkip:(x+RadPix)
            a=xPix-x;
            b=yPix-y;
            if (((yPix-y)^2+(xPix-x)^2)<=(RadPix^2))
               PixMat(xPix,yPix)=BTime1;
               PixMat((x-a),yPix)=BTime1;
               PixMat(xPix,(y-b))=BTime1;
               PixMat((x-a),(y-b))=BTime1;
            end
         end
```

```
        end
    end
end
x=XX;
x1=(ArrayMid/2)+RadPix;
ArrayMid=x1+(XX-x1)/2;

for m=(x+(PerPix/2)):(PerPix/2):4096
    for xPix=(m-RadPix):PSkip:(m+RadPix)
        for yPix=10:PSkip:4096
            PixMat(xPix,yPix)=BTime2;
            X=xPix-ArrayMid;
            if ((ArrayMid-X)>0)
            PixMat((ArrayMid-X),yPix)=BTime2;
            end
        end
    end
end

% Number of pixels to be milled: To be less than a million
PixCount=0;

for x=1:4096
    for y=1:4096
        if (PixMat(x,y)>0)
            PixCount=PixCount+1;
        end
    end
end
```

```
OutFile=strcat('PBRGR',int2str(Rad),'P',int2str(Per),'BT1',int2str(BTime1),'BT2',int2st
r(BTime2),'.str');
fid=fopen(OutFile,'w+');
fprintf(fid,'%c \n%u \n','s',5);
fprintf(fid,'%u \n',PixCount);
for x=1:4096
   for y=1:4096
      if (PixMat(x,y)>0)
         fprintf(fid,'%u \t %u \t %u \n',PixMat(x,y),x,y);
      end
   end
end
fclose(fid);
```

Script file for array with dimple PBR on two sides

```
%%%%%%%%%%%%%%%%%%%%%%%%%%%%%%%%%%%%%%%%%%%%%%%%%%%%%%%%%%%%%%%%%%%%%%%%%%%%%%%%
% Filename: PBRScript.m
% Author: Pramodha Marthandam
% Date created: 12 June 2007
% Structure details: Array of circular holes, about 15nmX15nm, surrounded
% by dimples, with half the periodicity of the hole array
%%%%%%%%%%%%%%%%%%%%%%%%%%%%%%%%%%%%%%%%%%%%%%%%%%%%%%%%%%%%%%%%%%%%%%%%%%%%%%%%


%Defining the nanometer to pixel conversion factor
NPixCon=7.14;

% Pixel Matrix
PixMat = zeros(4096,4096,'uint16');

% Opening the file input.txt and reading dimensional parameters
```

```
num = textread('input.txt','%u%*[^\n]');

% Extracting the parameters from the input file

% Hole diameter
Dia=num(1);

% Resonance wavelength (periodicity)
Per=num(2);

% Dwell times of hole and grating
BTime1=num(3);
BTime2=num(4);

% Pixel skip factor
PSkip=num(5);

% Conversion from nanometers to pixels
DiaPix=uint16(Dia/NPixCon);
RadPix=DiaPix/2;
PerPix=uint16(Per/NPixCon);

Rad=uint16(Dia/2);
ArrayMid=4096/2;

XX=0;
for y=(10+RadPix):PerPix:4096
   for x=(ArrayMid/2 +RadPix):PerPix:(ArrayMid+(ArrayMid/2))
      PixMat(x,y)=BTime1;
      if (x>XX)
         XX=x;
```

```
        end
        for yPix=y:PSkip:(y+RadPix)
            for xPix=x:PSkip:(x+RadPix)
                a=xPix-x;
                b=yPix-y;
                if (((yPix-y)^2+(xPix-x)^2)<=(RadPix^2))
                    PixMat(xPix,yPix)=BTime1;
                    PixMat((x-a),yPix)=BTime1;
                    PixMat(xPix,(y-b))=BTime1;
                    PixMat((x-a),(y-b))=BTime1;
                end
            end
        end
    end
end
x=XX;
x1=ArrayMid/2 +RadPix;
ArrayMid=x1+(XX-x1)/2;

for mx=(x+(PerPix/2)):(PerPix/2):4096
    for my=(10+RadPix):(PerPix):4096
        for xPix=mx:PSkip:(mx+RadPix)
            for yPix=my:PSkip:(my+RadPix)
                a=xPix-mx;
                b=yPix-my;
                if (((yPix-my)^2+(xPix-mx)^2)<=(RadPix^2))
                    if ((((2*ArrayMid)-(mx-a))>0) && (((2*ArrayMid)-xPix)>0))
                    PixMat(xPix,yPix)=BTime2;
                    PixMat(((2*ArrayMid)-xPix),yPix)=BTime2;
                    PixMat((mx-a),yPix)=BTime2;
                    PixMat(((2*ArrayMid)-(mx-a)),yPix)=BTime2;
```

```
                PixMat(xPix,(my-b))=BTime2;
                PixMat(((2*ArrayMid)-xPix),(my-b))=BTime2;
                PixMat((mx-a),(my-b))=BTime2;
                PixMat(((2*ArrayMid)-(mx-a)),(my-b))=BTime2;
                end
            end

        end
    end
end

PixCount=0;

for x=1:4096
    for y=1:4096
        if (PixMat(x,y)>0)
            PixCount=PixCount+1;
        end
    end
end

OutFile=strcat('PBRDR',int2str(Rad),'P',int2str(Per),'BT1',int2str(BTime1),'BT2',int2st
r(BTime2),'.str');
fid=fopen(OutFile,'w+');
fprintf(fid,'%c \n%u \n','s',5);
fprintf(fid,'%u \n',PixCount);
for x=1:4096
    for y=1:4096
        if (PixMat(x,y)>0)
            fprintf(fid,'%u \t %u \t %u \n',PixMat(x,y),x,y);
```

```
        end
    end
end
fclose(fid);
```

Input file for PBR structure

```
150  : Hole diameter (nm)
800  : resonance wavelength (periodicity)
3000 : Hole dwell time (ns)
100   : Grating dwell time (ns)
2    : Pixel skip
```

Appendix C

Script file for PBR all around the array

```
%%%%%%%%%%%%%%%%%%%%%%%%%%%%%%%%%%%%%%%%%%%%%%%
% Filename: PBRScript.m
% Author: Pramodha Marthandam
% Date created: 13 Sept 2007
% Structure details: Array of circular holes, about 15umX15um, surrounded
% by gratings, with half the periodicity of the hole array
%%%%%%%%%%%%%%%%%%%%%%%%%%%%%%%%%%%%%%%%%%%%%%%


%Defining the nanometer to pixel conversion factor
NPixCon=7.14;

% Pixel Matrix
PixMat = zeros(4096,4096,'uint16');

% Opening the file input.txt and reading dimensional parameters
num = textread('input.txt','%u%*[^\n]');

% Extracting the parameters from the input file

% Hole diameter
Dia=num(1);

% Resonance wavelength (periodicity)
Per=num(2);

% Dwell times of hole and grating
BTime1=num(3);
```

```
BTime2=num(4);

% Pixel skip factor
PSkip=num(5);

% Conversion from nanometers to pixels
DiaPix=uint16(Dia/NPixCon);
RadPix=DiaPix/2;
PerPix=uint16(Per/NPixCon);

Rad=uint16(Dia/2);
ArrayMid=4096/2;

XX=0;
YY=0;
for y=uint16(ArrayMid-ArrayMid/2 +RadPix):PerPix:(ArrayMid+(ArrayMid/2))
   for x=uint16(ArrayMid-ArrayMid/2 +RadPix):PerPix:(ArrayMid+(ArrayMid/2))
      PixMat(x,y)=BTime1;
      if (x>XX)
         XX=x;
      end
      if (y>YY)
         YY=y;
      end
      for yPix=y:PSkip:(y+RadPix)
         for xPix=x:PSkip:(x+RadPix)
            a=xPix-x;
            b=yPix-y;
            if (((yPix-y)^2+(xPix-x)^2)<=(RadPix^2))
               PixMat(xPix,yPix)=BTime1;
               PixMat((x-a),yPix)=BTime1;
```

```
                PixMat(xPix,(y-b))=BTime1;
                PixMat((x-a),(y-b))=BTime1;
            end
        end
    end
  end
end
x=XX;
y=YY;
x1=(ArrayMid/2)+RadPix;
ArrayMid=x1+(XX-x1)/2;

xStep=uint16(PerPix/2 *cos(45*pi/180));
yStep=uint16(PerPix/2 *sin(45*pi/180));
xMin=uint16(ArrayMid-ArrayMid/2 +RadPix);
yMin=xMin;
xMax=x+xStep;
yMax=y+yStep;

ym1=uint16(ArrayMid-(YY-ArrayMid));
ym2=YY;
PSkip=PSkip+1;
for xpix=uint16(XX+PerPix/2):uint16(PerPix/2):4096
  xm=uint16(ArrayMid-(xpix-ArrayMid));
  l=xpix-ArrayMid;
  yl1=ArrayMid-l;
  yl2=ArrayMid+l;
  for x1=(xpix-RadPix):PSkip:(xpix+RadPix)
    for y1=(yl1-RadPix):PSkip:(yl2+RadPix)
      if (x1>0 && y1>0)
        PixMat(x1,y1)=BTime2;
```

```
            a=y1-ArrayMid;
            y2=uint16(ArrayMid-a);
            b=x1-ArrayMid;
            x2=uint16(ArrayMid-b);
            if (x2>0 && y2>0)
               PixMat(x2,y2)=BTime2;
               PixMat(x1,y2)=BTime2;
               PixMat(x2,y1)=BTime2;
            end
         end
      end
   end
end

xm1=uint16(ArrayMid-(XX-ArrayMid));
xm2=XX;

for ypix=uint16(YY+PerPix/2):uint16(PerPix/2):4096
      l=ypix-ArrayMid;
      xl1=ArrayMid-l;
      xl2=ArrayMid+l;
      for y1=(ypix-RadPix):PSkip:(ypix+RadPix)
         for x1=(xl1-RadPix):PSkip:(xl2+RadPix)
            if (x1>0 && y1>0)
               PixMat(x1,y1)=BTime2;
               %PixMat(y1,x1)=BTime2;
               a=x1-ArrayMid;
               x2=uint16(ArrayMid-a);
               b=y1-ArrayMid;
               y2=uint16(ArrayMid-b);
               if (x2>0 && y2>0)
```

```
                PixMat(x2,y2)=BTime2;
                %PixMat(y2,x2)=BTime2;
                PixMat(x1,y2)=BTime2;
                PixMat(x2,y1)=BTime2;
                %PixMat(y2,x1)=BTime2;
                %PixMat(y1,x2)=BTime2;
                end
            end
        end
    end
    xm1=uint16(xm1-PerPix/2);
    xm2=uint16(xm2+PerPix/2);
end


PixCount=0;

for x=1:4096
    for y=1:4096
        if (PixMat(x,y)>0)
            PixCount=PixCount+1;
        end
    end
end

OutFile=strcat('PBRR',int2str(Rad),'P',int2str(Per),'BT1',int2str(BTime1),'BT2',int2str(
BTime2),'.str');
fid=fopen(OutFile,'w+');
fprintf(fid,'%c \n%u \n','s',6);
fprintf(fid,'%u \n',PixCount);
for x=1:4096
```

```
    for y=1:4096
        if (PixMat(x,y)>0)
            fprintf(fid,'%u \t %u \t %u \n',PixMat(x,y),x,y);
        end
    end
end
fclose(fid);

PixCount2=0;

for x=1:4096
    for y=1:4096
        if (PixMat(x,y)==BTime1)
            PixCount2=PixCount2+1;
        end
    end
end

OutFile=strcat('ArrayR',int2str(Rad),'P',int2str(Per),'BT1',int2str(BTime1),'BT2',int2str
(BTime2),'.str');
fid=fopen(OutFile,'w+');
fprintf(fid,'%c \n%u \n','s',6);
fprintf(fid,'%u \n',PixCount2);
for x=1:4096
    for y=1:4096
        if (PixMat(x,y)==BTime1)
            fprintf(fid,'%u \t %u \t %u \n',PixMat(x,y),x,y);
        end
    end
end
fclose(fid);
```

```
PixCount3=0;

for x=1:4096
   for y=1:4096
      if (PixMat(x,y)==BTime2)
         PixCount3=PixCount3+1;
      end
   end
end

OutFile=strcat('REFR',int2str(Rad),'P',int2str(Per),'BT1',int2str(BTime1),'BT2',int2str(
BTime2),'.str');
fid=fopen(OutFile,'w+');
fprintf(fid,'%c \n%u \n','s',6);
fprintf(fid,'%u \n',PixCount3);
for x=1:4096
   for y=1:4096
      if (PixMat(x,y)==BTime2)
         fprintf(fid,'%u \t %u \t %u \n',PixMat(x,y),x,y);
      end
   end
end
fclose(fid);
```

Input file for PBR all around the array

```
150  : Hole diameter (nm)
800  : resonance wavelength (periodicity)
3000 : Hole dwell time (ns)
50   : Grating dwell time (ns)
```

2 : Pixel skip

Appendix D

Script file for quasicrystal structure

```
%%%%%%%%%%%%%%%%%%%%%%%%%%%%%%%%%%%%%%%%%%%%%%%%%
% Filename: Penrose.m
% Author: Pramodha Marthandam
% Date created: 13 July 2007
% Structure details: Penrose tiling with five fold rotational symmetry
% by gratings, with half the periodicity of the hole array
%%%%%%%%%%%%%%%%%%%%%%%%%%%%%%%%%%%%%%%%%%%%%%%%%
%Defining the nanometer to pixel conversion factor
NPixCon=7.14;

% Opening the file input.txt and reading dimensional parameters
num = textread('input.txt','%u%*[^\n]');

dia=num(1);
BTime=num(2);
PSkip=num(3);

rad=uint16(dia/2);
% Conversion from nm to pixel
DiaPix=uint16(dia/NPixCon);
RadPix=uint16(rad/NPixCon);



pm_raw=zeros (465,622,'uint16');
for x=1:465
    for y=1:622
        if (cdata(x,y)==0)
            for xx=(x-3):(x+3)
```

```
            for yy=(y-3):(y+3)
               if (xx>0 && yy>0)
               cdata(xx,yy)=1;
               end
            end
         end
         cdata(x,y)=0;
      end
   end
end
for x=1:465
   for y=1:622
      if (cdata(x,y)==0)
         pm_raw(x,y)=1;
      end
   end
end

sc700x=uint16(3102/465);
sc700y=uint16(4102/622);


sc800x=uint16(3542/465);
sc800y=uint16(4685/622);

sc900x=uint16(3981/465);
sc900y=uint16(5267/622);


pm700=zeros(4096,4096,'uint16');
```

```
pm800=zeros (4096,4096,'uint16');

pm900=zeros (4096,4096,'uint16');

for x=1:465
   for y=1:622
      if (pm_raw(x,y)==1)


         if (((20+(x*sc800x)) <4096) && ((20+(y*sc800y ))<4096))
            pm800((20+(x*sc800x)),(20+(y*sc800y)))=5*pm_raw(x,y);
         end

         if (((20+(x*sc700x)) <4096) && (((20+y*sc700y ))<4096))
            pm700((20+(x*sc700x)),(20+(y*sc700y)))=5*pm_raw(x,y);
         end
         if (((20+(x*sc900x))<4096) && ((20+(y*sc900y )<4096)))
            pm900((20+(x*sc900x)),((20+(y*sc900y))))=5*pm_raw(x,y);
         end


      end
   end
end

for X=1:4096
   for Y=1:4096
      if (pm800(X,Y)==5)
            for xPix=X:PSkip:(X+RadPix)
               for yPix=Y:PSkip:(Y+RadPix)
                  a=xPix-X;
                  b=yPix-Y;
```

```
                if (((xPix-X)^2 + (yPix-Y)^2)<= (RadPix^2))
                   if ((X-a)>0 && (Y-b)>0)
                      pm800(xPix,yPix)=1;
                      pm800((X-a),yPix)=1;
                      pm800(xPix,(Y-b))=1;
                      pm800((X-a),(Y-b))=1;
                   end
                end
             end
          end
       end
    end
end

for X=1:4096
   for Y=1:4096
      if (pm900(X,Y)==5)
            for xPix=X:PSkip:(X+RadPix)
               for yPix=Y:PSkip:(Y+RadPix)
                  a=xPix-X;
                  b=yPix-Y;
                  if (((xPix-X)^2 + (yPix-Y)^2)<= (RadPix^2))
                     if ((X-a)>0 && (Y-b)>0)
                        pm900(xPix,yPix)=1;
                        pm900((X-a),yPix)=1;
                        pm900(xPix,(Y-b))=1;
                        pm900((X-a),(Y-b))=1;
                     end
                  end
               end
            end
```

```
      end
   end
end

for X=1:4096
   for Y=1:4096
      if (pm700(X,Y)==5)
            for xPix=X:PSkip:(X+RadPix)
               for yPix=Y:PSkip:(Y+RadPix)
                  a=xPix-X;
                  b=yPix-Y;
                  if (((xPix-X)^2 + (yPix-Y)^2)<= (RadPix^2))
                     if ((X-a)>0 && (Y-b)>0)
                        pm700(xPix,yPix)=1;
                        pm700((X-a),yPix)=1;
                        pm700(xPix,(Y-b))=1;
                        pm700((X-a),(Y-b))=1;
                     end
                  end
               end
            end
      end
   end
end

PixCount700=0;
PixCount800=0;
PixCount900=0;

for x=1:4096
   for y=1:4096
```

```
        if (pm700(x,y)>0)
            PixCount700=PixCount700+1;
        end
    end
end

OutFile=strcat('QCR',int2str(rad),'SP700.str');
fid=fopen(OutFile,'w+');
fprintf(fid,'%c \n%u \n','s',1);
fprintf(fid,'%u \n',PixCount700);
for x=1:4096
    for y=1:4096
        if (pm700(x,y)>0)
            fprintf(fid,'%u \t %u \t %u \n',BTime,x,y);
        end
    end
end
fclose(fid);

for x=1:4096
    for y=1:4096
        if (pm800(x,y)>0)
            PixCount800=PixCount800+1;
        end
    end
end

OutFile=strcat('QCR',int2str(rad),'SP800.str');
fid=fopen(OutFile,'w+');
fprintf(fid,'%c \n%u \n','s',1);
fprintf(fid,'%u \n',PixCount800);
```

```
for x=1:4096
   for y=1:4096
      if (pm800(x,y)>0)
         fprintf(fid,'%u \t %u \t %u \n',BTime,x,y);
      end
   end
end
fclose(fid);

for x=1:4096
   for y=1:4096
      if (pm900(x,y)>0)
         PixCount900=PixCount900+1;
      end
   end
end

OutFile=strcat('QCR',int2str(rad),'SP900.str');
fid=fopen(OutFile,'w+');
fprintf(fid,'%c \n%u \n','s',1);
fprintf(fid,'%u \n',PixCount900);
for x=1:4096
   for y=1:4096
      if (pm900(x,y)>0)
         fprintf(fid,'%u \t %u \t %u \n',BTime,x,y);
      end
   end
end
fclose(fid);
```

Appendix E

Polystyrene self assembly

The experiment presented below did not yield satisfactory results. This section is presented for the benefit of those attempting self-assembly on gold substrates. Self assembly of polystyrene spheres (PS) was attempted to find a way to controllably fabricate arrays of nano-holes. An aqueous suspension PS of 1μm diameter, with a standard deviation of 0.14μm was used. The PS colloid was purchased from Bangs Labs Inc. Various dilutions of the master suspension (10% by weight) were made to find out which concentration yielded a self assembled mono-layer (SAM).

A dilution of 0.001% by volume of the master suspension in ultra-pure water yielded a single layer PS. Figure E1 shows an SEM of the gold slide with a single layer of PS. Fairly good ordering of PS is seen. However, due to hydrophobic nature of the gold surface, proper wetting of surface was never achieved. Due to this, clumping of PS within the mono-layer is seen. Most literature shoes formations PS SAMs on hydrophilic materials.

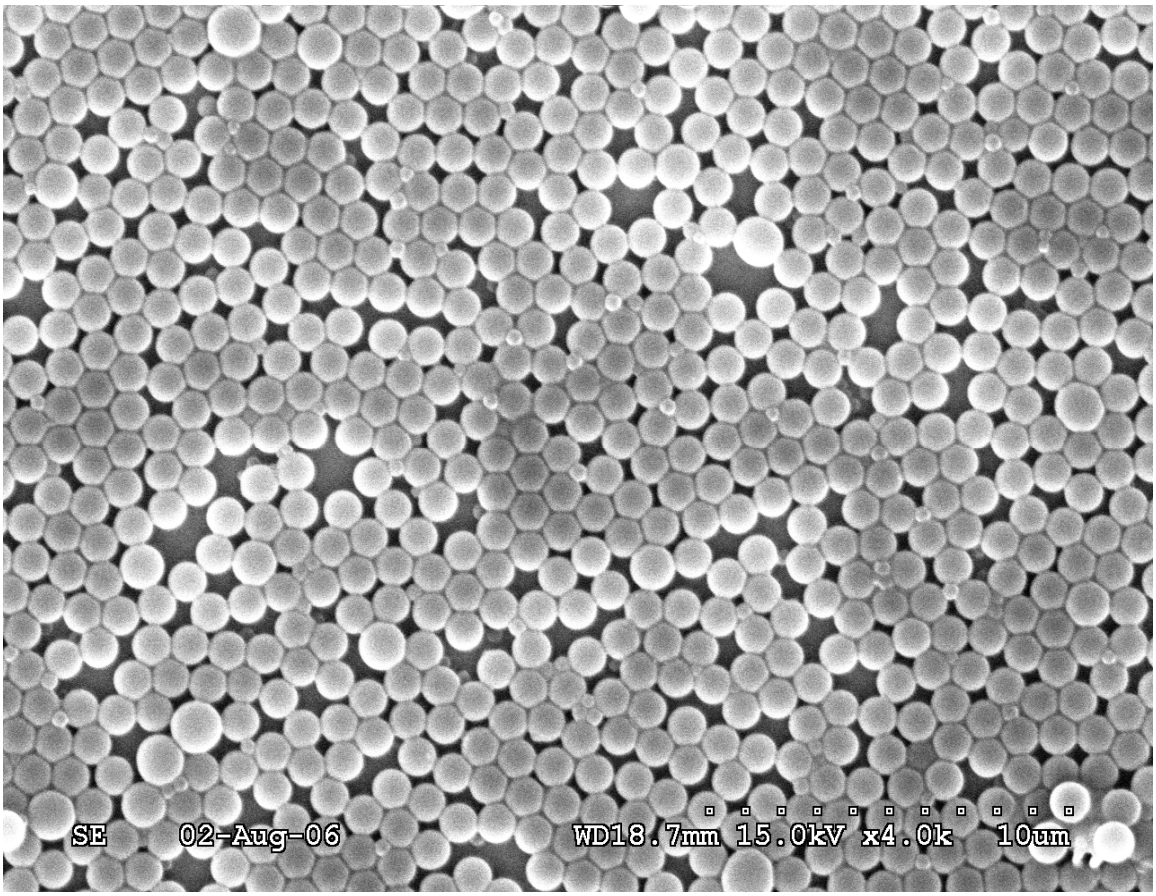

Figure E1: SEM of 0.001% of PS. Single layer formation is seen.

A combination of bottom-up approach of PS self assembly and top-down approach of FIB was attemped. In order to obtain an ordered assembly of PS, a series of grooves of width 1μm were milled using FIB. The thickness of the gold film used was 100 nm, and the diameter of PS was 1μm. Due to the fact that a 100 nm trough was too shallow for holding the PS, proper settling os PS in etched grooves was not achieved.

Appendix F

Optical trapping with nano-hole arrays

The experiment outlined below did not yield satisfactory results. It is documented for the benefit of future attempts.

Due to the high field intensities at the surface of a metal film arising from SPR of nano-hole arrays, it is possible that trapping of dielectric particles can occur. Optical trapping of PS of diameter 1μm was attempted using arrays of double holes milled on a gold on glass slide. The double hole arrays were used because they have high local field intensities at the apexes. Five arrays with periodicities 380 nm, 430 nm, 490 nm, 545 nm and 580 nm were used with a He-Ne laser (λ=632.8 nm). The laser was incident on the glass substrate side. PS suspension was dropped on the gold side, and a cover slip was dropped to enable imaging of the gold slide using a CCD camera.

Figure F1 shows a schematic of the setup used in the trapping experiments. When the laser is turned on, it is incident on the nano-hole arrays. When the periodicity of array, and the SPR coincide with the laser wavelength, a strong electric field is expected to be setup on the surface, This field is expected to have an exponential decay away from the gold surface. This evanescent field will cause trapping of particles in the array.

The experimental data recorded was the number of particles in within the array versus time. Figure F2 shows the number of particles within the array versus time. Before the laser is turned on, there few particles within the array. A random drift of particles in the suspension was seen. A balance was observed between particles entering the array, and particles leaving the array. Once the laser was turned on, particles were seen to be attracted towards the array. The number of particles entering the array was seen to be greater than the number leaving it. This led to a buildup of particles in the array. After a certain time, the number of particles in the array is seen to reach a saturaion level, beyond which no further increase was seen.

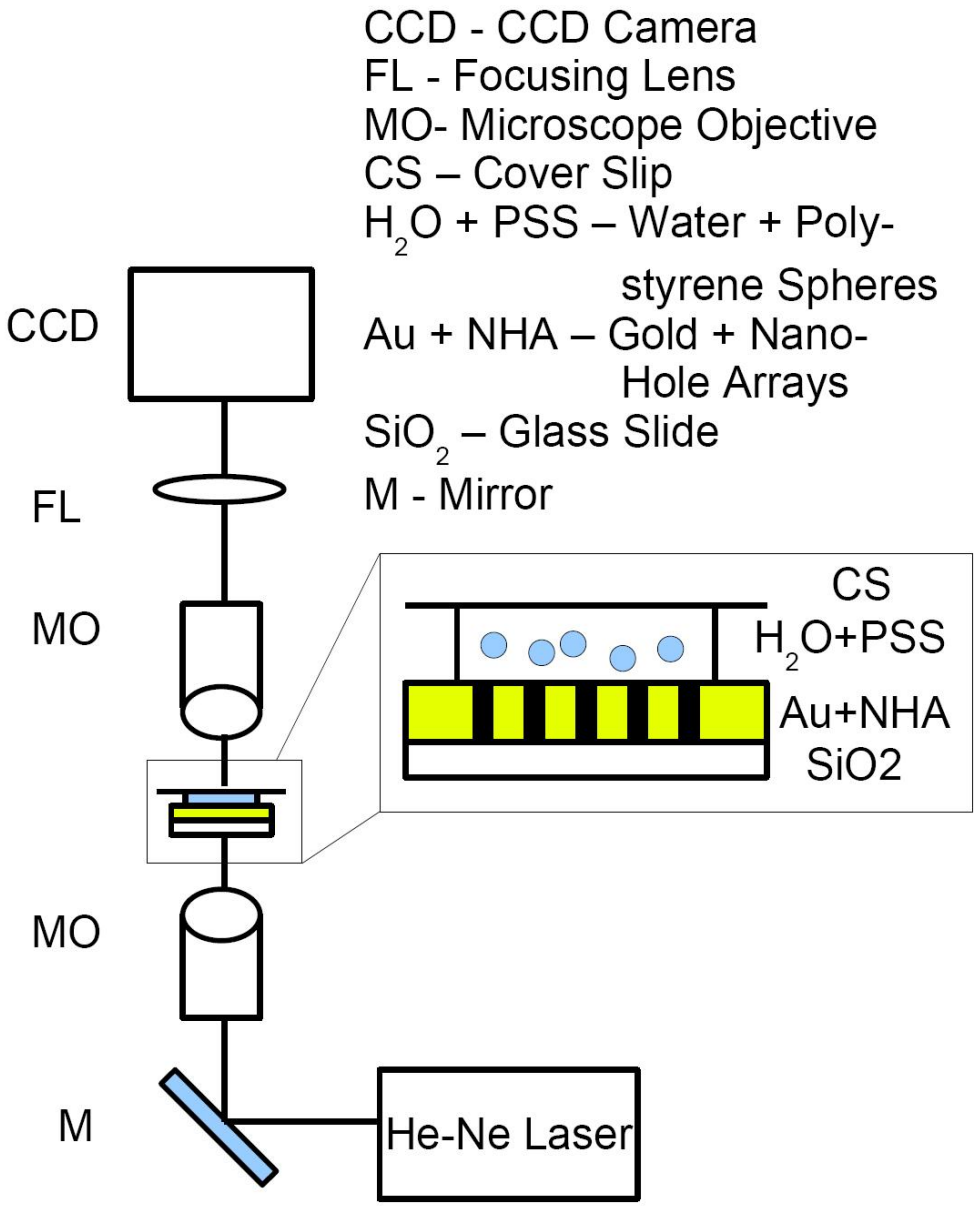

Figure F1: Schematic of trapping setup.

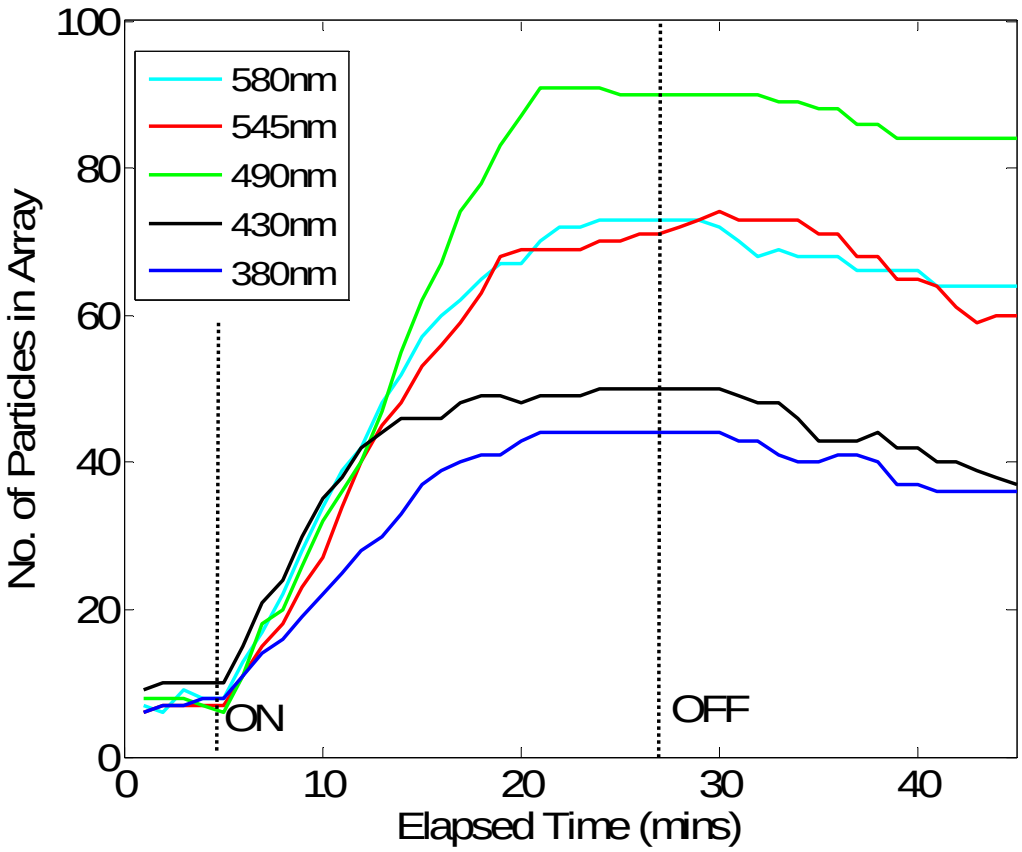

Figure F2: Particle buildup in the array with time, when laser is on. An initial increase in the number of particles in the array, followed by a saturation, and subsequent decrease is seen.

Although a buildup was seen, with this data, and experimental conditions, conclusions could not be drawn as to the mechanism behind the particle buildup. The imaging of the CCD showed agglomeration of particles within the boundaries of the array, but the resolution was insufficient to determine whether the spheres were attracted to the gold surface due to SP fields, or to the cover slips due to the hydrophobic nature of PS.